

# FAR-INFRARED TO MILLIMETER DATA OF PROTOPLANETARY DISKS: DUST GROWTH IN THE TAURUS, OPHIUCHUS, AND CHAMAELEON I STAR-FORMING REGIONS\*.

ÁLVARO RIBAS<sup>1</sup>, CATHERINE C. ESPAILLAT<sup>1</sup>, ENRIQUE MACÍAS<sup>1</sup>, HERVÉ BOUY<sup>2</sup>, SEAN ANDREWS<sup>3</sup>, NURIA CALVET<sup>4</sup>, DAVID A. NAYLOR<sup>5</sup>, PABLO RIVIERE-MARICHALAR<sup>6</sup>, MATTHIJS H. D. VAN DER WIEL<sup>5, 7</sup>, AND DAVID WILNER<sup>3</sup>

<sup>1</sup>Department of Astronomy, Boston University, Boston, MA 02215, USA; aribas@bu.edu

<sup>2</sup>Laboratoire d'Astrophysique de Bordeaux, Univ. Bordeaux, CNRS, F-33615 Pessac, France

<sup>3</sup>Harvard-Smithsonian Center for Astrophysics, Cambridge, MA 91023 USA

<sup>4</sup>Astronomy Department, University of Michigan, Ann Arbor, MI 48109, USA

<sup>5</sup>Institute for Space Imaging Science, Department of Physics & Astronomy, University of Lethbridge, Canada

<sup>6</sup>Instituto de Ciencia de Materiales de Madrid (CSIC). Calle Sor Juana Inés de la Cruz 3, E-28049 Cantoblanco, Madrid, Spain

<sup>7</sup>ASTRON, the Netherlands Institute for Radio Astronomy, PO Box 2, 7990AA Dwingeloo, The Netherlands

## ABSTRACT

Far-infrared and (sub)millimeter fluxes can be used to study dust in protoplanetary disks, the building blocks of planets. Here, we combine observations from the *Herschel Space Observatory* with ancillary data of 284 protoplanetary disks in the Taurus, Chamaeleon I, and Ophiuchus star-forming regions, covering from the optical to mm/cm wavelengths. We analyze their spectral indices as a function of wavelength and determine their (sub)millimeter slopes when possible. Most disks display observational evidence of grain growth, in agreement with previous studies. No correlation is found between other tracers of disk evolution and the millimeter spectral indices. A simple disk model is used to fit these sources, and we derive posterior distributions for the optical depth at 1.3 mm and 10 au, the disk temperature at this same radius, and the dust opacity spectral index  $\beta$ . We find the fluxes at 70  $\mu\text{m}$  to correlate strongly with disk temperatures at 10 au, as derived from these simple models. We find tentative evidence for spectral indices in Chamaeleon I being steeper than those of disks in Taurus/Ophiuchus, although more millimeter observations are needed to confirm this trend and identify its possible origin. Additionally, we determine the median spectral energy distribution of each region and find them to be similar across the entire wavelength range studied, possibly due to the large scatter in disk properties and morphologies.

*Keywords:* protoplanetary disks — stars: pre-main sequence — infrared: general — submillimeter: general

## 1. INTRODUCTION

Planetary systems form out of disks of gas and dust around young stars. However, the large number of physical processes taking place within them (e.g., accretion, photoevaporation, interaction with companions, dust growth and settling, radial migration, Takeuchi & Lin 2002; D'Alessio et al. 2006; Ireland & Kraus 2008; Alexander et al. 2014) require that we consider several factors for their study. For this purpose, multi-wavelength observations of protoplanetary disks can be used to better understand their properties.

The (sub)mm wavelength range is of particular inter-

est for various reasons: at sufficiently long wavelengths, disks become optically thin, and an estimate of their dust mass can be directly obtained (via some assumptions) by simply measuring their flux (e.g. Beckwith et al. 1990). Although the bulk of the disk mass in the system is in gaseous phase, fiducial (or measured, when available) gas-to-dust ratios provide an indirect estimate of the total mass in the disk. This is a crucial parameter for planet formation theories because it determines the available reservoir for this process. Using this method, surveys of star-forming regions with (sub)mm facilities such as SMA and ALMA have determined that protoplanetary disks have typical masses of 0.1-0.5 % of that of their host star (e.g. Andrews & Williams 2005; Andrews et al. 2013; Pascucci et al. 2016). On the other hand, dust growth represents the initial stage of planet formation; the observed spectral index at these wave-

\**Herschel* is an ESA space observatory with science instruments provided by European-led Principal Investigator consortia and with important participation from NASA.

lengths can be linked to the dust opacity in the disk, informative of its properties and grain sizes (e.g. Miyake & Nakagawa 1993; Draine 2006). In fact, the comparison of the millimeter spectral index of the interstellar medium (ISM) with that of protoplanetary disks has already revealed significant dust growth in these disks, implying the presence of mm/cm-sized grains in many of them (e.g. D’Alessio et al. 2001; Lommen et al. 2010; Ricci et al. 2010b,a; Ubach et al. 2012). The combination of the mm spectral index with additional information at other wavelengths, such as the spectral index at near/mid infrared (IR) wavelengths or silicate features may also point to links between the evolution of the inner and outer regions of the disks. As an example, Lommen et al. (2010) identified a tentative correlation between the strength of the  $10\ \mu\text{m}$  silicate feature and the 1-3 mm spectral index for a sample of T Tauri and Herbig Ae/Be stars, suggesting a connection between the evolution of the inner and outer regions of disks, although a later study by Ricci et al. (2010a) found no signs of such a correlation for disks in the Taurus and Ophiuchus star-forming regions. Despite the obvious interest of this wavelength regime, disks have relatively weak emission at millimeter wavelengths and many of them currently lack this type of data (or, at least, sufficient observations to provide robust estimates of their spectral indices).

At somewhat shorter wavelengths, the *Herschel Space Observatory* (Herschel, Pilbratt et al. 2010) observed large areas of the sky in the far-IR and sub-mm, including several star-forming regions (e.g. the Gould Belt Survey, André et al. 2010). *Herschel* probed the range between 50 and  $150\ \mu\text{m}$ , which is sensitive to dust settling (e.g. D’Alessio et al. 2006), but also provided fluxes at longer wavelengths (up to  $\sim 700\ \mu\text{m}$ ) probing deeper into the disk mid-plane. Various studies have already analyzed different aspects of *Herschel* data in star-forming regions, both from the photometric (e.g. Winston et al. 2012; Howard et al. 2013; Olofsson et al. 2013; Ribas et al. 2013; Spezzi et al. 2013; Bustamante et al. 2015; Rebollido et al. 2015) and spectroscopic (Cieza et al. 2013; Dent et al. 2013; Riviere-Marichalar et al. 2016) points of view. On the other hand, a large comparative analysis of *Herschel* data of protoplanetary disks in different star-forming regions is still missing.

In this work, we compile multi-wavelength data of protoplanetary disks, including homogeneous *Herschel* photometry and spectroscopy, in three nearby star-forming region: Taurus (1-2 Myr and  $\sim 140$  pc, Torres et al. 2007; Andrews et al. 2013), Ophiuchus (0.3-5 Myr and  $\sim 140$  pc, Wilking et al. 2008; Ortiz-León et al. 2017), and Chamaeleon I (2-6 Myr and  $\sim 160$  pc, Whittet et al. 1997; Luhman 2007). The proximity of these regions and

the amount of available ancillary data guarantee good coverage of the spectral energy distributions (SEDs) of several of their disks. Sec. 2 describes our sample, data compilation, and processing. In Sec. 3 we analyze different aspects of (sub)mm spectral indices and investigate observational evidence of dust growth in these SEDs. In Sec. 4, we provide further analysis by fitting the compiled data with a simple disk model. Sec. 5 discusses and compares the median SEDs of these regions. Finally, our conclusions are presented in Sec. 6.

## 2. SAMPLE AND DATA COMPILATION

Our goal was to compile a representative sample of the disk population in the Taurus, Ophiuchus, and Chamaeleon I molecular clouds, while also ensuring a good coverage of their SEDs from the optical to the far-IR, as well as the millimeter range when possible. We considered the 161 Taurus objects studied by Furlan et al. (2011), 134 objects in Ophiuchus in McClure et al. (2010), and the 84 objects in Chamaeleon I analyzed in Manoj et al. (2011). These studies presented and analyzed *Spitzer*/IRS spectra of these disks, and performed a detailed study of the properties of their inner regions. They also provided homogeneous compilations of the stellar properties of these objects. Based on this and our intention to model these sources in more detail in a future study, we selected these three sub-samples as our initial sample. To avoid disks with significant contribution from their envelopes, we discarded envelope-dominated SEDs (as identified in these studies), which were present both in the Ophiuchus and Chamaeleon I samples. Our final sample comprises 315 objects: 161 in Taurus, 83 in Ophiuchus, and 71 in Chamaeleon I.

### 2.1. *Herschel* data

Due to the different methods used to process *Herschel* data in various studies and the inherent difficulties of obtaining photometric and spectroscopic measurements in the presence of conspicuous background emission (the cold dust in molecular clouds emits strongly at far-IR wavelengths), a coherent comparison of these data is complex and has not yet been explored. To guarantee a homogeneous data set, observations of the three regions were processed in the same manner.

#### 2.1.1. *Herschel* Photometry

We processed a number of scan and cross scan maps available in the *Herschel* Science Archive to achieve a satisfactory coverage of the three regions considered in this study. All of them were obtained by the the *Herschel* Gould Belt Survey (P.I.: Philippe André), except for one set of observations in Ophiuchus (P.I.: Peter Abraham). The corresponding OBSIDs, instruments, wavelengths, and pointing coordinates are summarized

in Table A1 in Appendix A. After this process, a total number of 18 objects in our sample lie outside the coverage of the large maps used in this study. For these, we queried the *Herschel* Science Archive to retrieve additional (smaller) observations that contained these objects. We found PACS detections for 11 of these sources. The corresponding OBSIDs and information for these data are also listed in Appendix A.

Maps at the three PACS wavelengths (70, 100, and 160  $\mu\text{m}$ ) were processed using the *JScanam* algorithm (Graciá-Carpio et al. 2015) within HIPE (Herschel Interactive Processing Environment, Ott 2010) version 14, combining scan and cross scan maps. In the particular case of OBSIDs 1342202254 (scan), 1342202090 (cross scan 1) and 1342190616 (cross scan 2), these three maps cover the same region of the sky, but *JScanam* can only process scan + cross scan pairs. For this reason, we produced two different maps with each scan and cross scan combination. We then extracted PACS aperture photometry at the nominal coordinates of each object with the *annular sky aperture photometry* task within HIPE, using aperture radii of 15", 18", and 22" for 70, 100, and 160  $\mu\text{m}$ , respectively. These values were determined to be a good compromise based on inspection of growth curves obtained in scan + cross scan maps. The background was estimated within an annulus with radii of 25" and 35" centered around each object. We then applied the corresponding aperture correction factors with the *photApertureCorrectionPointSource* task, corresponding to 0.83, 0.84, and 0.82 for 70, 100, and 160  $\mu\text{m}$ , respectively. Given the different slopes of Class II SEDs in the PACS regime, we chose not to apply color corrections to these fluxes—which, in any case, are significantly smaller than the assumed uncertainties (see below).

SPIRE photometry was obtained at the three available wavelengths (250, 350, and 500  $\mu\text{m}$ ) using the recommended procedure of fitting sources in the timeline (Pearson et al. 2014) within HIPE. The level 1 data were previously corrected using the *destriper* task. No extended emission gains were applied because we do not expect any of these disks to be resolved in *Herschel*/SPIRE maps at their corresponding distances. The timeline fitting method does not require aperture corrections, but we did apply color corrections in this case; at the longer SPIRE wavelengths, disks are (at least partly) optically thin, and their emission at these wavelengths can therefore be fitted with a power law. Based on mm spectral indexes by Ricci et al. (2010b), we used an intermediate power-law index of 2.3 and applied the corresponding color corrections. The uncer-

tainty from this parameter is, in any case, of only a few percent<sup>1</sup>.

Reliable source detection in *Herschel* maps of star-forming regions is a challenging task, given the strong (and usually highly structured) background emission. We therefore performed visual inspection of each source in all the available wavelengths to guarantee that we only include clean point source detections. We discarded every source/band with extended objects, significant contribution by nearby sources or the emission from the molecular clouds, or tentative/non detections. For objects covered by more than one map, the median flux value was adopted. To account for the effect of the aforementioned conspicuous background at *Herschel* wavelengths, based on previous *Herschel* studies (e.g. Ribas et al. 2013; Rebollido et al. 2015), we assigned a conservative 20% uncertainty to each *Herschel* photometric measurement. The resulting photometry, together with objects that were discarded during the visual inspection process, are listed in Appendix B.

### 2.1.2. *Herschel*/SPIRE Spectroscopy

We also obtained SPIRE Fourier Transform Spectrometer (FTS) low-resolution ( $\lambda/\Delta\lambda = 48$  at 250  $\mu\text{m}$ ) spectra for 113 objects (P.I.: Catherine Espaillat, proposal ID: OT1\_cespaill\_1). These data cover wavelengths from 190 to 670  $\mu\text{m}$ , and were processed within HIPE 14 using the standard pipeline (Fulton et al. 2016), which also reduces the long-wavelength artifacts produced when operating the SPIRE FTS in low-resolution mode (Marchili et al. 2017). In addition to standard processing, background subtraction is crucial at long wavelengths in star-forming regions. We inspected all SPIRE detectors for each object to discard undetected sources, and removed those on top of isolated strong background emission that could yield an overestimation of the true background flux. Once a reliable estimate of the background flux was established, it was subtracted from the detector viewing the source. We applied the pointing offset correction within HIPE (Valtchanov et al. 2014) when possible, in order to mitigate discontinuities between the two spectral windows. The extremities of the spectra were then trimmed to avoid the lower S/N regions. Finally, the resulting spectra were compared with SPIRE data and archival photometry (see next section), and we discarded those with obvious discrepancies with the photometry, mostly due to decreasing signal to noise with increasing wavelengths. Thirty-four clean SPIRE spectra remained after this process, and are available in the online version. The obsids of both clean and discarded SPIRE FTS spectra are listed in Appendix A.

<sup>1</sup> [http://herschel.esac.esa.int/Docs/SPIRE/spire\\_handbook.pdf](http://herschel.esac.esa.int/Docs/SPIRE/spire_handbook.pdf)

Table 1. Catalogs and Surveys Used in this Study

Catalog/Survey	Telescope/Instrument(s)	Wavelength range	Region	<sup>a</sup>	Reference
Sloan Digital Sky Survey (DR9)	SDSS telescope	0.35 - 0.91 $\mu\text{m}$	...		Ahn et al. (2012)
AAVSO Photometric All Sky Survey (APASS)	Multiple telescopes	0.44 - 0.76 $\mu\text{m}$	...		Henden et al. (2016)
Carlsberg Meridian Catalog (DR15)	CMT	0.62 $\mu\text{m}$	...		...
Two Micron All Sky survey (2MASS)	2MASS	1.24 - 2.16 $\mu\text{m}$	...		Skrutskie et al. (2006)
Wide Infrared Explorer (WISE)	WISE	3.4 - 22 $\mu\text{m}$	...		Wright et al. (2010)
Cores to disks (c2d) survey	Spitzer/IRAC, MIPS	3.6 - 24 $\mu\text{m}$	Taurus, Ophiuchus		Evans et al. (2009)
AKARI mid-infrared survey	AKARI/IRC	9 - 18 $\mu\text{m}$	...		Ishihara et al. (2010)
-	ALMA	887 $\mu\text{m}$	Taurus		Ricci et al. (2014)
-	IRAM Plateau de Bure Interferometer	3.2 mm	Taurus		Piétu et al. (2014)
-	SCUBA/JCMT + literature	350 $\mu\text{m}$ - 1.3 mm	Ophiuchus		Andrews & Williams (2007)
-	ALMA	890 $\mu\text{m}$	Ophiuchus		Testi et al. (2016)
-	ATCA	3.3 mm	Ophiuchus		Ricci et al. (2010a)
-	VLA	4 - 7 cm	Ophiuchus		Dzib et al. (2013)
-	Spitzer/IRAC, MIPS	3.4 - 24 $\mu\text{m}$	Chamaeleon I		Luhman et al. (2008)
-	SEST	1.3 mm	Chamaeleon I		Henning et al. (1993)
-	APEX/LABOCA	870 $\mu\text{m}$	Chamaeleon I		Belloche et al. (2011)
-	ALMA	887 $\mu\text{m}$	Chamaeleon I		Pascucci et al. (2016)
-	ATCA	3 mm - 6 cm	Chamaeleon I		Ubach et al. (2012)

<sup>a</sup>Only for region-specific surveys.

NOTE—The majority of the data for Taurus objects were gathered from the compilation in Andrews et al. (2013), and we refer the reader to this study for additional information.

## 2.2. Archival data

To complement *Herschel* data, we queried a number of catalogs for photometry covering a broad wavelength range. In the case of Taurus, data from the comprehensive compilation by [Andrews et al. \(2013\)](#) was used when available. Ancillary photometry in the range of 60-160  $\mu\text{m}$  was found to be significantly noisy (possibly due to the lower resolution and sensitivity of previous facilities/telescopes), and was excluded because *Herschel* data are now available. For the remaining Taurus objects, as well as for Ophiuchus and Chamaeleon, we cross-matched our sample with a number of surveys and catalogs, listed in Table 1. The cross-match was performed by assigning the fluxes to the closest source within a radius of  $3''$ , except for APEX/LABOCA, SCUBA, or VLA, where a  $5''$  search radius was used due to their larger beam sizes.

We paid special attention to saturation magnitudes and the various flags (such as objects marked as extended) in different observations. It is likely that some of the compiled data suffer from undetected additional problems (e.g., contamination by nearby sources) that may affect our analysis, particularly in the (sub)mm domain; we therefore inspected each SED visually and discarded any photometric point clearly inconsistent with the overall shape of the SED. This process also helps to identify and discard possible mismatches in the cross-matching process.

*Spitzer*/IRS ([Houck et al. 2004](#)) spectra of these objects were also retrieved from the Cornell Atlas of *Spitzer*/IRS Sources (CASSIS, [Lebouteiller et al. 2011, 2015](#)). CASSIS produces optimally extracted spectra (accounting for e.g. pointing shifts in the slit, local background), which are suitable for our purposes. However, for some sources, we find issues in the automatic reduction by CASSIS (e.g. non-matching orders); in those cases we used the spectra from [Furlan et al. \(2011\)](#), [McClure et al. \(2010\)](#), and [Manoj et al. \(2011\)](#). If several spectra were available in CASSIS, we visually inspected them and chose those that better matched our compiled photometry, given that the mid-IR emission of disks can be variable (e.g. [Espaillat et al. 2011](#); [Morales-Calderón et al. 2011](#)). Furthermore, we do not include the spectrum for T Tau, given the strong neighboring background emission and its inconsistency with the compiled SED.

To our knowledge, this is the largest data compilation to date for Chamaeleon I and Ophiuchus. An example of one of the compiled, clean SEDs is presented in Table 2. The whole data set (SEDs and available SPIRE and IRS spectra) is available for download in tar.gz packages. In addition, the entire data set is available in a Zenodo archive [[10.5281/zenodo.889053](https://doi.org/10.5281/zenodo.889053)].

**Table 2.** Example of One of the Observed (Not De-reddened) SEDs<sup>a</sup>: WX Cha

Wavelength ( $\mu\text{m}$ )	$F_\nu$ (mJy)	Reference
0.44	$4.5 \pm 0.9$	<a href="#">Henden et al. (2016)</a>
0.48	$6 \pm 1$	<a href="#">Henden et al. (2016)</a>
0.55	$11 \pm 2$	<a href="#">Henden et al. (2016)</a>
0.62	$19 \pm 4$	<a href="#">Henden et al. (2016)</a>
0.76	$35 \pm 4$	<a href="#">Henden et al. (2016)</a>
1.23	$186 \pm 5$	<a href="#">Skrutskie et al. (2006)</a>
1.66	$320 \pm 10$	<a href="#">Skrutskie et al. (2006)</a>
2.16	$432 \pm 7$	<a href="#">Skrutskie et al. (2006)</a>
3.6	$450 \pm 20$	<a href="#">Luhman et al. (2008)</a>
4.5	$450 \pm 20$	<a href="#">Luhman et al. (2008)</a>
4.6	$430 \pm 10$	<a href="#">Wright et al. (2010)</a>
5.8	$400 \pm 20$	<a href="#">Luhman et al. (2008)</a>
8.0	$400 \pm 20$	<a href="#">Luhman et al. (2008)</a>
9.0	$440 \pm 20$	<a href="#">Murakami et al. (2007)</a>
12	$370 \pm 20$	<a href="#">Wright et al. (2010)</a>
18	$420 \pm 30$	<a href="#">Murakami et al. (2007)</a>
22	$410 \pm 20$	<a href="#">Wright et al. (2010)</a>
24	$390 \pm 20$	<a href="#">Luhman et al. (2008)</a>
70	$330 \pm 70$	This work
100	$220 \pm 40$	This work
160	$180 \pm 40$	This work
160	$120 \pm 20$	This work
250	$100 \pm 20$	This work
350	$110 \pm 20$	This work
500	$120 \pm 20$	This work
887	$21 \pm 2$	<a href="#">Pascucci et al. (2016)</a>

<sup>a</sup>The IRS spectrum is available in the online version of the manuscript.

NOTE—Similar datasets, including *Spitzer*/IRS and *Herschel*/SPIRE spectra are available for each of the considered sources in the online version of the manuscript.

## 2.3. De-reddening and stellar parameters

The data were de-reddened using  $A_V$  values for Ophiuchus ([McClure et al. 2010](#)) and  $A_J$  values for Taurus and Chamaeleon I ([Furlan et al. 2011](#); [Manoj et al. 2011](#)). We followed the procedure adopted in [McClure et al. \(2010\)](#) to select the extinction law to be used for each target:

1. For  $A_V < 3$ , we use the extinction law in [Mathis \(1990\)](#) with  $R_V = 3.1$ .



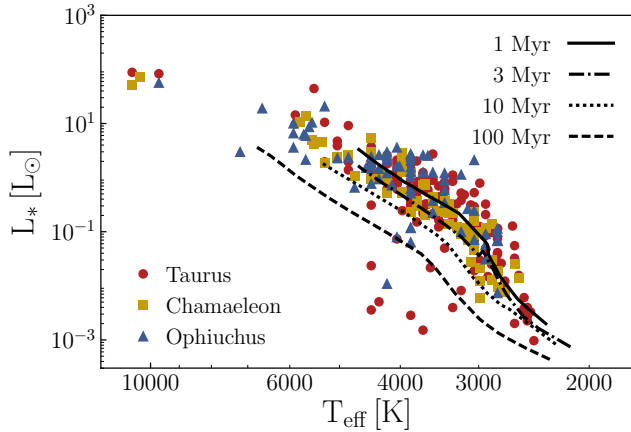


**Figure 1.** HR diagram of the sample. Taurus objects are shown as red circles, Chamaeleon as yellow squares, and Ophiuchus members as blue triangles. Underluminous sources are likely YSOs with edge-on disks, self-extincting their stellar radiation. Isochrones from Baraffe et al. (2015) are also shown for comparison.

2. For cases  $3 \leq A_V < 8$  and  $A_V > 8$ , we use the corresponding the extinction laws in McClure (2009).

In the following, sources with  $A_V \geq 15$  are excluded from the analysis: these objects are either highly embedded in their parental cloud or located behind a significant amount of dust. In both cases, their spectral types (SpTs) are more uncertain, and such large extinctions may create important features in the SED shape that could alter the result of our analysis. Moreover, the obscuring dust will emit at longer wavelengths (longward of far-IR), and both *Herschel* photometry and ancillary data may be contaminated by this emission. After this stage of the analysis, the sample size has been reduced to 284 YSOs: 154 in Taurus, 70 in Ophiuchus, and 60 in Chamaeleon I.

To assign stellar parameters, we used SpTs listed in Furlan et al. (2011), McClure et al. (2010), and Manoj et al. (2011). These were translated into stellar effective temperatures ( $T_{\text{eff}}$ ) using the updated SpT– $T_{\text{eff}}$  relation in Pecaut & Mamajek (2013). We then scaled the corresponding BT-Settl photospheres (Allard et al. 2012) to the de-reddened 2MASS  $J$  fluxes and computed the luminosities by integrating them in wavelength space at each region distance. The resulting HR-diagram of the whole sample is shown in Fig. 1. The adopted stellar parameters are available in the online version of the manuscript, and a reduced version can be found in Table 3.

### 3. MILLIMETER SPECTRAL INDICES AND EVIDENCE FOR GRAIN GROWTH

The emission from protoplanetary disks at a given wavelength depends on several factors, such as their morphology, dust composition, and stellar host prop-

erties. In particular, the (sub)mm emission is informative of the mass and characteristics of dust in disks. In this section, we investigate the observational evidence for grain growth in the compiled data.

#### 3.1. Spectral indices versus wavelength

Observations of protoplanetary disks in the (sub)mm range have two particularities: they probe the Rayleigh Jeans (RJ) regime of the emission (unless the disk is abnormally cold), and the opacity at these wavelengths is low enough for disks to be mostly optically thin. When these two conditions are met (and assuming a power-law dependence of the opacity with frequency), changing the wavelength does not affect the spectral index ( $\alpha$ ) of the SED, and the emission from the disk follows  $F_\nu \propto \nu^\alpha$ . We computed this spectral index ( $\alpha = d \log F_\nu / d \log \nu$ ) at eight different wavelength ranges for objects in the sample to investigate when it becomes independent of  $\lambda$ . The wavelength ranges and corresponding  $\alpha$  median values are listed in Table 4. These slopes were measured for each object with two or more data points available in the corresponding range. Absolute  $\alpha$  values larger than five were discarded because they are unphysical (very likely they are the result of individual problematic data). Figure 2 shows the obtained probability distribution for each of these ranges<sup>2</sup>. As expected, the median values increase significantly from one range to the next for the shorter wavelength ranges, and the distributions become very similar for  $\alpha_{880-1.3}$  and  $\alpha_{1.3-5}$  despite the significant change in wavelength. This suggests that the aforementioned conditions (RJ regime and optically thin emission) are met for most disks in this range, as typically assumed. The distribution of  $\alpha_{500-880}$  is also close to those of  $\alpha_{880-1.3}$  and  $\alpha_{1.3-5}$ , implying that the deviations from these conditions are small (at least for some disks) at these wavelengths.

#### 3.2. Measuring millimeter spectral indices

A significant number of protoplanetary disks lack enough (sub)mm data to estimate  $\alpha_{\text{mm}}$ . As suggested by Fig. 2, it is possible that the large amounts of SPIRE observations in the *Herschel* Science Archive could be used as an additional data set for this purpose, at the cost of introducing some (systematic) uncertainty due to deviations from the RJ regime or optically thick emission at these wavelengths.

The compiled data were used to quantify the deviation from the “true”  $\alpha_{\text{mm}}$  value produced by including SPIRE photometry in its measurement. The “true”

<sup>2</sup> We prefer Gaussian Kernel Density Estimates (KDEs) over histograms, when possible, to present distributions, because the latter are sensitive to the choice of origin and widths of bins.

Table 3. Adopted Stellar Parameters for the Presented Sample

Name	R.A. (hh:mm:ss.ss)	Decl. (dd:mm:ss.ss)	Adopted. SpT	Adopted. Teff (K)	Lum ( $L_{\odot}$ )	$A_v$ (mag)	Region
2MASS J04141188+2811535	04:14:11.88	+28:11:53.5	M6.25	2760	2.6e-02	2.5	Taurus
2MASS J04153916+2818586	04:15:39.16	+28:18:58.6	M3.75	3250	3.3e-01	2.5	Taurus
2MASS J04155799+2746175	04:15:57.99	+27:46:17.5	M5.5	2920	8.4e-02	1.9	Taurus
2MASS J04163911+2858491	04:16:39.12	+28:58:49.1	M5.5	2920	4.6e-02	3.0	Taurus
2MASS J04201611+2821325	04:20:16.11	+28:21:32.6	M6.5	2720	9.3e-03	0.8	Taurus
2MASS J04202144+2813491	04:20:21.44	+28:13:49.2	M1	3680	1.5e-03	0.0	Taurus
2MASS J04202606+2804089	04:20:26.07	+28:04:09.0	M3.5	3300	1.6e-01	0.0	Taurus
2MASS J04210795+2702204	04:21:07.95	+27:02:20.4	M5.25	2990	3.0e-02	4.5	Taurus
2MASS J04214631+2659296	04:21:46.31	+26:59:29.6	M5.75	2860	2.7e-02	4.2	Taurus
2MASS J04230607+2801194	04:23:06.07	+28:01:19.5	M6	2800	3.8e-02	0.7	Taurus
2MASS J04242090+2630511	04:24:20.90	+26:30:51.2	M6.5	2720	1.2e-02	0.8	Taurus
2MASS J04242646+2649503	04:24:26.46	+26:49:50.4	M5.75	2860	2.5e-02	1.3	Taurus
2MASS J04263055+2443558	04:26:30.55	+24:43:55.9	M8.75	2480	3.3e-03	0.2	Taurus
2MASS J04284263+2714039	04:28:42.63	+27:14:03.9	M5.25	2990	1.2e-01	3.9	Taurus
2MASS J04290068+2755033	04:29:00.68	+27:55:03.4	M8.25	2540	6.1e-03	0.2	Taurus
2MASS J04295950+2433078	04:29:59.51	+24:33:07.8	M5	3050	2.4e-01	4.8	Taurus
2MASS J04322415+2251083	04:32:24.15	+22:51:08.3	M4.5	3120	8.6e-02	1.3	Taurus
2MASS J04330945+2246487	04:33:09.46	+22:46:48.7	M6	2800	4.1e-02	3.6	Taurus
2MASS J04333905+2227207	04:33:39.05	+22:27:20.7	M1.75	3580	2.2e-02	0.0	Taurus
2MASS J04334465+2615005	04:33:44.65	+26:15:00.5	M4.75	3090	3.1e-01	5.4	Taurus

NOTE—The complete version of Tables 3, 5, 6, and B5 are merged together in the Zenodo repository, also available in machine readable format in the online journal

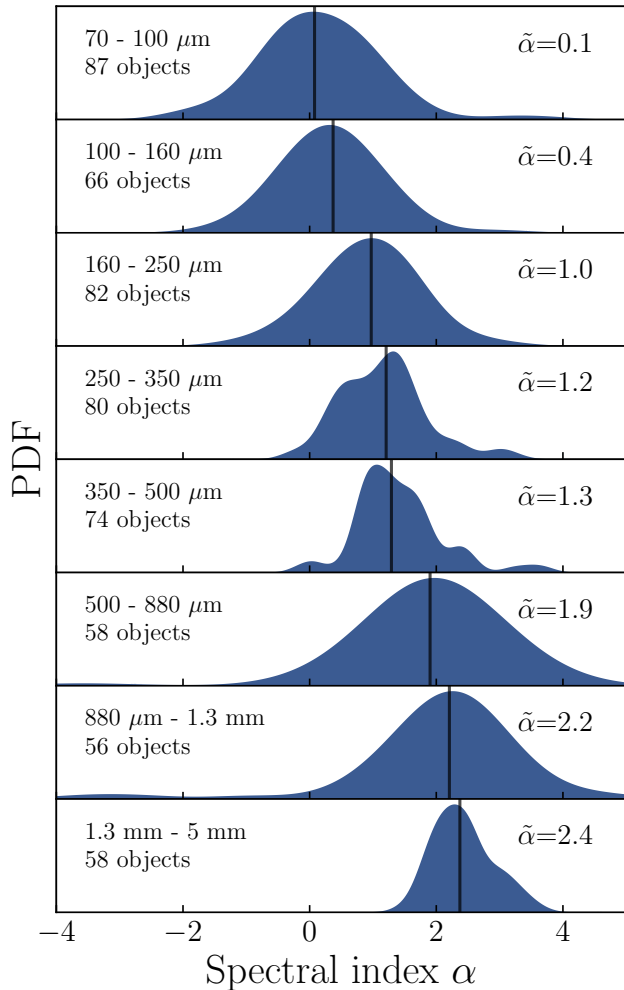


**Figure 2.** Probability density functions (PDFs) of the SED slopes ( $\alpha$ ) of considered sources measured at different wavelength ranges. The number of objects in each distribution and the median  $\alpha$  values ( $\tilde{\alpha}$ , and black vertical line) are indicated in each case. Distributions shift to larger  $\alpha$  values for increasing wavelengths, as emission approaches the Rayleigh Jeans regime and disks gradually become optically thin.

spectral index ( $\alpha_{\text{mm,true}}$ ) was defined as the slope determined with all the available data between  $700 \mu\text{m}$  and  $5 \text{ mm}$ ; these wavelengths are long enough to be mostly optically thin and in the RJ regime, yet they include little contribution from other mechanisms such as free-free or chromospheric emission (Pascucci et al. 2012). We computed  $\alpha_{\text{mm,true}}$  (when possible) for objects with at least three measurements in this wavelength range, in order to make our estimates more robust against any problematic data point that could have a significant effect in the results. We then computed spectral indices at four different wavelength ranges to quantify their deviation from the  $\alpha_{\text{mm,true}}$ . The four wavelength ranges included:

1. SPIRE 250, 350, and 500 data,

2. SPIRE 250, 350, and 500 data + available photometry between  $700 \mu\text{m}$  and  $5 \text{ mm}$
3. SPIRE 350, and 500 data + available photometry between  $700 \mu\text{m}$  and  $5 \text{ mm}$ , and
4. SPIRE 500 data + available photometry between  $700 \mu\text{m}$  and  $5 \text{ mm}$

Values were obtained only for sources with at least three available data points in the quoted regimes. The deviations of the different  $\alpha_{\text{mm}}$  values with respect to  $\alpha_{\text{mm,true}}$  were computed as:

$$\text{Deviation} = 100 \times \left( \frac{\alpha_{\text{mm,range}}}{\alpha_{\text{mm,true}}} - 1 \right) \quad (1)$$

where  $\alpha_{\text{mm,range}}$  is the slope measured for each of the four considered cases. The results are shown in Fig. 3. Deviations are largest when using SPIRE data only (ranging from  $-93\%$  to  $7\%$ , and with a median value of  $-53\%$ ), as expected since this is the shortest wavelength range considered. For cases combining SPIRE data with (sub)mm photometry from  $700 \mu\text{m}$  to  $5 \text{ mm}$  (as used to estimate  $\alpha_{\text{true,mm}}$ ), the most accurate values are obtained excluding short SPIRE bands because the considered fluxes become closer to the optically thin and RJ regimes. In particular, combining SPIRE  $500 \mu\text{m}$  photometry only with (sub)mm data yields a median deviation of only  $6\%$ , and in no case more than  $25\%$ .

**Table 4.** Median Spectral Indices Computed at Different Wavelength Ranges

Wavelength Range ( $\mu\text{m}$ )	Spectral Index	N. Objects
65-105	$0.1^{+0.9}_{-0.7}$	87
95-165	$0.4^{+0.7}_{-0.7}$	66
155-255	$1.0^{+0.7}_{-0.7}$	82
245-355	$1.2^{+0.5}_{-0.7}$	80
345-505	$1.3^{+0.6}_{-0.4}$	74
495-890	$1.9^{+0.9}_{-0.7}$	58
860-1400	$2.2^{+0.7}_{-0.9}$	56
1200-5000	$2.4^{+0.6}_{-0.4}$	58

NOTE—Uncertainties are derived from 16th and 84th percentiles.

Based on these results, we chose to estimate millimeter slopes  $\alpha_{\text{mm}}$  in the following manner:

1. For objects with at least two data points between  $800 \mu\text{m}$  and  $5 \text{ mm}$ , those data were used to estimate  $\alpha_{\text{mm}}$ .



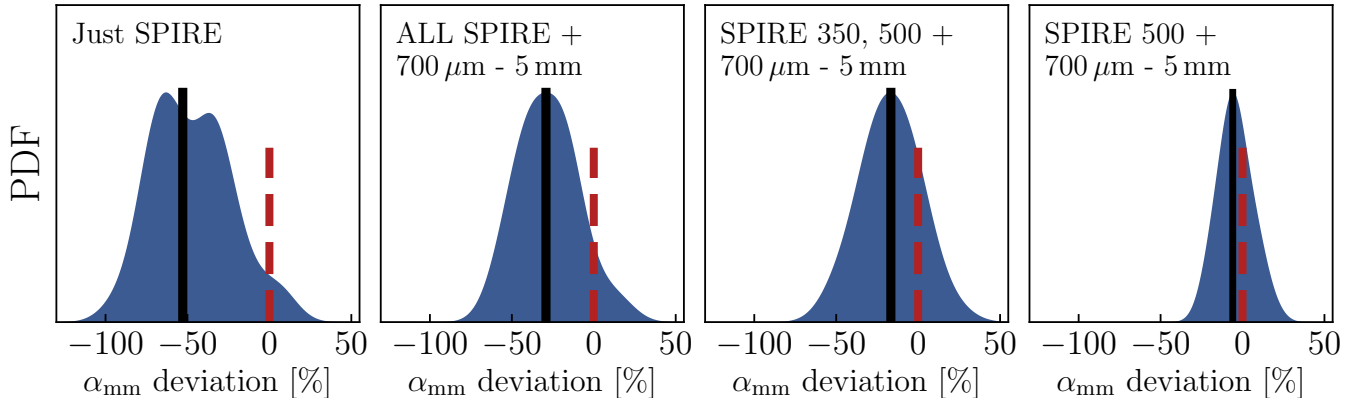


**Figure 3.** Probability density functions (PDF) of deviation from the “true” millimeter slope  $\alpha_{\text{mm,true}}$  (measured between  $700\ \mu\text{m}$  and  $5\ \text{mm}$ ) for spectral indices computed in the four considered ranges: using SPIRE data only (left), using all SPIRE data + photometry between  $700\ \mu\text{m}$  and  $5\ \text{mm}$  (middle left), SPIRE  $350 + \text{SPIRE } 500 + \text{photometry between } 700\ \mu\text{m}$  and  $5\ \text{mm}$  (middle right), and combining only SPIRE  $500\ \mu\text{m}$  with photometry between  $700\ \mu\text{m}$  and  $5\ \text{mm}$  (right). The median value of each distribution ( $-53\%$ ,  $-29\%$ ,  $-17\%$ , and  $-6\%$ , respectively) is shown as a black line, and the ideal case (no deviation) is shown as a red dashed line for reference. As expected, including shorter wavelengths in the analysis yields larger deviation in  $\alpha_{\text{mm}}$  estimates.

2. For objects without enough data in the previous case, but with at least two data points between  $500$  and  $5\ \text{mm}$ ,  $\alpha_{\text{mm}}$  was computed in that range, provided that at least one of the existing measurements was taken at wavelengths  $\geq 1\ \text{mm}$ .
3. In all cases, the separation between the minimum and maximum available wavelengths was required to be at least  $100\ \mu\text{m}$  to avoid issues when only two close measurements are available.

With this criterion, millimeter spectral indices for 78 objects were obtained, as listed in Table 5. One problematic source, CU Cha (one of the two Herbig Ae/Be stars in Chamaeleon I), was found to have a surprisingly high mm spectral index of 4.8. This value was computed using fluxes at  $870\ \mu\text{m}$  and  $1.3\ \text{mm}$  from Belloche et al. (2011) and Henning et al. (1993), and we were unable to identify any obvious problem in its SED. Such an  $\alpha$  value is unlikely to be real (e.g. D’Alessio et al. 2001; Ricci et al. 2010b), and no other source in our sample has a slope as steep as this object. More recent (sub)mm observations of this target by Walsh et al. (2016), using

ALMA, obtained a totally different value of  $\alpha_{\text{mm}}$  value of 0.3 (unphysical for thermal emission in the millimeter), but they encountered calibration issues during the observations and this value is highly uncertain. Later, van der Plas et al. (2017) quoted an  $\alpha$  value of 3.1 measured from 1 to  $10\ \text{mm}$  by including additional archival ATCA observations, which is more similar to other values in Chamaeleon. For consistency, we chose to leave this source outside the analysis.

The median of the distribution of millimeter spectral indices is 2.2, with values ranging from 1.5 to 3.5. On a region-by-region basis, median values and ranges are 2.2 (1.5-3.2) for Taurus (59 objects), 2.2 (1.7-3.3) for Ophiuchus (11 objects), and 3.0 (2.0-3.5) in Chamaeleon I (7 objects), in agreement with previous studies (e.g. Andrews & Williams 2007; Ricci et al. 2010a,b; Ubach et al. 2012; Andrews et al. 2013). The distribution of  $\alpha_{\text{mm}}$  is shown in Fig. 4. We note that the number of objects with measured spectral indices in Chamaeleon I and Ophiuchus is significantly smaller than in Taurus due to the lack of enough (sub)mm data for many of their sources, and these results should be considered with caution for these two regions.

**Table 5.** Adopted Millimeter Spectral Indices.

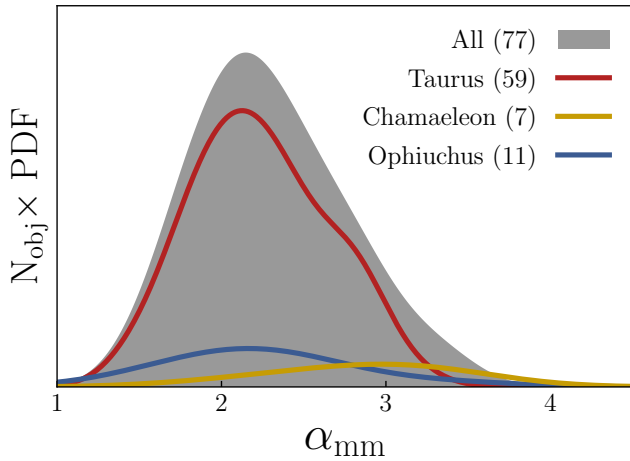
Name	$\alpha_{\text{mm}}$	Wavelength range ( $\mu\text{m}$ )	N. points
2MASS J04333905+2227207	$2.2^{+0.3}_{-0.3}$	500-1330	2
2MASS J04442713+2512164	$2.0^{+0.1}_{-0.1}$	869-3470	6
AA Tau	$2.0^{+0.2}_{-0.2}$	863-2700	8
AB Aur	$2.9^{+0.1}_{-0.1}$	850-2924	10

Table 5 continued

Table 5 (*continued*)

Name	$\alpha_{mm}$	Wavelength range ( $\mu\text{m}$ )	N. points
BP Tau	$2.7^{+0.2}_{-0.2}$	869-3400	6
CFHT 4	$2.1^{+0.1}_{-0.1}$	869-3220	6
CIDA 1	$2.0^{+0.2}_{-0.2}$	887-3220	3
CI Tau	$2.1^{+0.3}_{-0.3}$	869-2700	7
CW Tau	$2.9^{+0.2}_{-0.2}$	1056-3560	4
CX Tau	$2.3^{+0.2}_{-0.2}$	869-3477	3

NOTE—The complete version of Tables 3, 5, 6, and B5 are merged together in the Zenodo repository, also available in machine readable format in the online journal. Uncertainties are derived from the 16th and 84th percentile levels from MCMC analysis.



**Figure 4.** Distribution of millimeter SED slopes ( $\alpha_{mm}$ , measured between 500/800  $\mu\text{m}$  and 5 mm) for the sample. The overall distribution (gray), and the individual ones for Taurus (red), Chamaeleon I (yellow), and Ophiuchus (blue) are shown, scaled to the corresponding number of objects as indicated in the legend.

### 3.3. Dust growth in protoplanetary disks

As previously mentioned, (sub)mm fluxes and spectral indices of protoplanetary disks are related to their dust mass and properties. Under some assumptions (i.e. that the wavelength is long enough for the disk to be optically thin, and that a single temperature  $T_c$  can be used to describe the emission at this wavelength), the observed flux can be approximated as (Hildebrand 1983; Beckwith et al. 1990):

$$F_\nu = \frac{B_\nu(T_c)M_d\kappa_\nu}{d^2} \quad (2)$$

where  $B_\nu(T)$  is the Planck function at the characteristic temperature  $T_c$ ,  $M_d$  is the dust mass of the disk,  $\kappa_\nu$  is the dust opacity at the considered wavelength, and  $d$  is the distance to the object. This has been routinely

used to estimate disk masses via (sub)mm surveys (e.g. Beckwith et al. 1990; Andre & Montmerle 1994; Andrews & Williams 2005, 2007; Andrews et al. 2013). In this equation, the opacity value  $\kappa_\nu$  is the main source of uncertainty, and the prescription of Beckwith et al. (1990) is typically adopted:

$$\kappa_\nu = \kappa_0 \left( \frac{\nu}{10^{12}\text{Hz}} \right)^\beta \text{ cm}^2\text{g}^{-1} \quad (3)$$

where  $\beta$  determines the change of the opacity with wavelength, and  $\kappa_0$  is the opacity value at 10<sup>12</sup> Hz ( $\kappa_0=0.01 \text{ cm}^2\text{g}^{-1}$  in Beckwith et al. 1990). If we also assume that (sub)mm observations probe the RJ regime of  $B_\nu(T)$ , then  $B_\nu(T) \propto \nu^2$  and the spectral index at these wavelengths is therefore:

$$\alpha = \frac{d \log F_\nu}{d \log \nu} = 2 + \beta \quad (4)$$

The interest of  $\beta$  is that it depends on the properties of dust, i.e. the particle size distribution (power-law index and maximum grain size  $a_{\text{max}}$ ) and composition (D’Alessio et al. 2001; Natta et al. 2004; Draine 2006; Natta et al. 2007; Ricci et al. 2010b). Therefore,  $\beta$  can be used to probe grain growth in protoplanetary disks (Testi et al. 2014), a crucial process in planet formation. For ISM-like grains ( $a_{\text{min}}=0.005 \mu\text{m}$ ,  $a_{\text{max}}=0.25 \mu\text{m}$ ,  $n(a) \propto a^{-p}$ ,  $p = 3.5$ , Mathis et al. 1977),  $\beta$  typically ranges between 1.6 and 1.8, whereas increasing the maximum grain size to mm or cm sizes decreases  $\beta$  to 0-1 (depending on the assumed power-law index). Low  $\beta$  values have been found in several protoplanetary disks (e.g. Calvet et al. 2002; Ricci et al. 2010a,b; Ubach et al. 2012), indicating dust growth from ISM sizes (Beckwith & Sargent 1991; Miyake & Nakagawa 1993; Natta et al. 2004).

For sources with enough data to estimate  $\alpha_{\text{mm}}$  (see

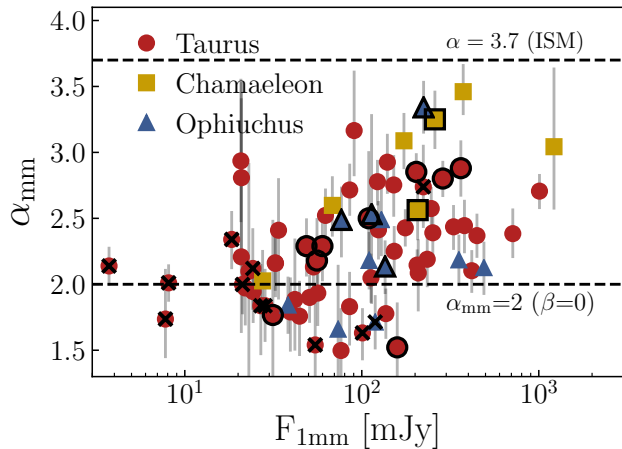


**Figure 5.** Predicted fluxes at 1 mm (scaled to 140 pc in the case of Chamaeleon I) vs. spectral indices in the millimeter for objects in Taurus (red), Chamaeleon I (yellow), and Ophiuchus (blue). M2 and later-type stars are marked with black crosses. Objects with a surrounding black border are classified as (pre)transitional disks by their 13-31  $\mu\text{m}$  spectral index. The  $\alpha=2$  line (corresponding to  $\beta=0$  in the Rayleigh Jeans regime and for optically thin disks) and the  $\alpha$  value of the ISM ( $\beta = 1.7$ ) are also shown.

Sec. 3.2), a line was fitted to their SEDs in  $\log \nu - \log F_\nu$  space to predict the fluxes at 1 mm for each source. Sources in Chamaeleon I were scaled to 140 pc to correct to its different distance (160 pc) with respect to Taurus and Ophiuchus. Figure 5 shows these 1 mm fluxes versus the corresponding  $\alpha_{\text{mm}}$  values. Our results are very similar to those found in previous studies (e.g. Ricci et al. 2010a,b; Testi et al. 2014). The lack of sources with low  $F_{1\text{mm}}$  and high  $\alpha_{\text{mm}}$  values is an observational bias: for a given  $F_{1\text{mm}}$ , higher  $\alpha_{\text{mm}}$  values result in more rapidly declining fluxes with increasing wavelength, and hence more challenging detections (Ricci et al. 2010b).

An inspection of Figs. 4 and 5 shows that most objects have  $\alpha_{\text{mm}}$  values between 2 and 3. Following Eq. 4, this implies that most disks have  $\beta \leq 1$ , pointing to grain growth processes in them. Given the young ages of sources in Ophiuchus and Taurus, this provides a robust confirmation (with a larger sample and homogeneous treatment) of the fact that grain growth from ISM-like to mm/cm sizes occurs quickly and early in the disk lifetimes, as already found in previous studies (e.g. Rodmann et al. 2006; Ricci et al. 2010b). The existence of objects with  $\alpha_{\text{mm}} < 2$  can not be explained with the relation  $\alpha = 2 + \beta$  because no physical dust model produces negative  $\beta$  values (e.g. D’Alessio et al. 2001;

Draine 2006). For those cases, it is likely that the assumption of the RJ regime does not hold: emission from disks with a very cold mid-plane (e.g. Guilloteau et al. 2016) may depart from  $F_\nu \propto \nu^2$  significantly, yielding flatter slopes. Late-type stars (considered here arbitrarily as M2 or later type, as a compromise; see crosses in Fig. 5) show  $\alpha_{\text{mm}}$  values below 2.5, with several of them even below 2. Although this may hint at important dust growth around low-mass stars and brown dwarfs, disks around these objects can be both colder and smaller than their counterparts in more massive stars, and therefore their emission could be optically thick and/or outside the RJ regime. Resolved observations are needed to unambiguously determine the origin of their low  $\alpha_{\text{mm}}$  values (see discussion in Ricci et al. 2014; Testi et al. 2016). Additionally, Chamaeleon I shows an excess of high  $\alpha_{\text{mm}}$  - high  $F_{1\text{mm}}$  fluxes with respect to Taurus and Ophiuchus, which is discussed later in the text (Sec. 4.3).

### 3.4. Millimeter indices and other tracers of disk evolution

Using the compiled data, we also searched for correlations of the mm slopes measured in Sec. 3.2 with other indicators of disk evolution; namely, the strength and shape of the 10  $\mu\text{m}$  silicate feature probing dust growth in the upper layers of disks, and tracers of cavities in them. The presence of gaps and cavities in the dust spatial distribution in disks was first inferred in their SEDs due to a deficit of near/mid-IR excess in some objects (Strom et al. 1989), and was later confirmed via direct imaging (e.g. Andrews et al. 2011). These particular disks with a hole are called transitional disks (or pre-transitional disks, if they have ring-like gaps separating their inner and outer regions), and they have gained significant attention in the last two decades due to the exciting possibility of these gaps/holes being produced by forming giant planets (see Espaillat et al. 2014, for a recent review). Because they lack material in their inner regions, their near/mid-IR emission is reduced and they have steeper SEDs at these wavelengths with respect to full disks, a fact that has been used in the past to identify transitional disk candidates (e.g. Forrest et al. 2004; Brown et al. 2007; Merín et al. 2010; McClure et al. 2010). The presence of giant planets directly implies that grains must have suffered significant growth, and hence it is possible that dust in transitional disks may have different properties. In the case of full disks, dust settling toward the disk mid-plane also decreases the IR emission, producing a change in their slopes at these wavelengths (e.g. Furlan et al. 2005).

**Table 6.** IR spectral indices and  $10\ \mu\text{m}$  silicate feature properties.

Name	$\alpha_{5.3-12.9}$	$\alpha_{12.9-31}$	Sil <sub>strength</sub>	Sil <sub>shape</sub>
2MASS J04141188+2811535	$-0.6^{+0.1}_{-0.1}$	$-0.57^{+0.08}_{-0.08}$	$0.6^{+0.2}_{-0.3}$	$0.94^{+0.07}_{-0.07}$
2MASS J04153916+2818586	$0.47^{+0.09}_{-0.08}$	$-1.43^{+0.07}_{-0.07}$	$0.11^{+0.08}_{-0.1}$	$0.96^{+0.08}_{-0.07}$
2MASS J04155799+2746175	$0.02^{+0.08}_{-0.08}$	$0.1^{+0.2}_{-0.1}$	$0.4^{+0.07}_{-0.11}$	$0.99^{+0.06}_{-0.05}$
2MASS J04163911+2858491	$0.5^{+0.2}_{-0.2}$	$0.0^{+0.2}_{-0.2}$	$0.1^{+0.2}_{-0.1}$	$1.0^{+0.1}_{-0.1}$
2MASS J04201611+2821325	$-0.01^{+0.08}_{-0.08}$	$0.0^{+0.4}_{-0.3}$	$0.05^{+0.09}_{-0.05}$	$0.92^{+0.05}_{-0.05}$
2MASS J04202144+2813491	$0.0^{+0.3}_{-0.2}$	$-1.2^{+0.3}_{-0.3}$	$-0.3^{+0.2}_{-0.2}$	$2.1^{+1.7}_{-0.6}$
2MASS J04202606+2804089	$-1.2^{+0.1}_{-0.1}$	$-1.39^{+0.06}_{-0.06}$	$1.4^{+0.2}_{-0.2}$	$0.92^{+0.05}_{-0.05}$
2MASS J04210795+2702204			$-0.1^{+0.7}_{-26.7}$	
2MASS J04214631+2659296	$-0.0^{+0.4}_{-0.4}$	$-0.2^{+3.2}_{-0.7}$	$0.2^{+0.7}_{-0.3}$	$0.9^{+0.3}_{-0.3}$
2MASS J04230607+2801194	$0.15^{+0.08}_{-0.07}$	$-0.9^{+0.1}_{-0.1}$	$0.24^{+0.14}_{-0.07}$	$0.92^{+0.06}_{-0.05}$

NOTE—The complete version of Tables 3, 5, 6, and B5 are merged together in the Zenodo repository, also available in machine readable format in the online journal. Uncertainties derived from 16th and 84th percentile levels from 1000 bootstrapping iterations.

Dust growth is thought to occur mostly in the disk mid-plane, where the density is higher and temperatures lower than in the upper layers (see the review in [Testi et al. 2014](#)), where the  $10\ \mu\text{m}$  silicate feature originates. Therefore, a relation between this feature and  $\alpha_{\text{mm}}$  would imply a co-evolution of grains in the upper layers of disks and their mid-plane. [Lommen et al. \(2007, 2010\)](#) found a tentative correlation between silicate strengths and shapes (a tracer of grain crystallinity) for YSOs in different star-forming regions, but [Ricci et al. \(2010a\)](#) did not find any in Ophiuchus. A later study by [Ubach et al. \(2012\)](#) revealed only a weak, also tentative correlation between the strength of this feature and the  $\alpha_{\text{mm}}$  for some sources in Taurus, Ophiuchus, Chamaeleon, and Lupus. We used the compiled IRS spectra (when possible) to compute silicate strengths and shapes following [Furlan et al. \(2006\)](#) and [Kessler-Silacci et al. \(2006\)](#) respectively. The resulting values are listed in Table 6, and the process is described in more detail in Appendix C. Spearman rank tests revealed no significant correlations between the strength/shape of the silicate feature and  $\alpha_{\text{mm}}$ , neither for any or these regions individually nor for the whole sample.

Near/mid-IR spectral indices  $\alpha_{\text{IR}}$  were also computed, following [McClure et al. \(2010\)](#), using the IRS spectra between 5.3 and  $12.9\ \mu\text{m}$  (taken as the median flux within a range of  $\pm 0.2\ \mu\text{m}$  centered around each of these wavelengths), and the slope between 12.9 and  $31\ \mu\text{m}$ . Spearman rank tests between  $\alpha_{\text{IR}}$  and  $\alpha_{\text{mm}}$  showed these two quantities to be uncorrelated, both for the whole sample and for each individual region. We also iden-

tified (pre)transitional disks by selecting objects with spectral indices between 13 and  $31\ \mu\text{m} < -1.4$  (in  $F_\nu$  space, as computed from their IRS spectra), following the criterion in [McClure et al. \(2010\)](#). These sources are encircled in Fig. 5 for comparison, but no obvious trend was found for them. These results suggest that the dust population in the midplane/outer regions of transitional disks (at least those which gaps have a detectable effect in the IR slope of their SEDs) is not substantially different than those of their full counterparts.

#### 4. A SIMPLE DISK MODEL

After the analysis of spectral indices in Sec. 3, we applied the simple disk model in [Beckwith et al. \(1990\)](#) to the compiled long-wavelength ( $\geq 70\ \mu\text{m}$ ) data. This model does not depict a physically self-consistent disk, but instead assumes that the emission arises from a vertically isothermal one. The SED of such a disk can be written as:

$$F_\nu = \frac{\cos i}{d^2} \int_{r_{in}}^{R_d} B_\nu(T(r))(1 - e^{-\tau_\nu(r) \sec i}) 2\pi r dr \quad (5)$$

where  $i$  is the inclination,  $d$  is the distance to the source,  $r_{in}$  and  $R_d$  are the inner and outer radii of the disk,  $B_\nu(T(r))$  is the Planck function at the temperature  $T(r)$ , and  $\tau_\nu(r)$  is the optical depth at the given frequency  $\nu$  and radius  $r$ . This optical depth is the product of the opacity at the corresponding frequency ( $\kappa_\nu$ ) and the radial surface density profile ( $\Sigma(r)$ ). We assume the radial dependence of the temperature and surface den-

sity to follow a power law:

$$T(r) = T_0 \left( \frac{r}{r_0} \right)^{-q} \quad (6)$$

$$\Sigma(r) = \Sigma_0 \left( \frac{r}{r_0} \right)^{-p} \quad (7)$$

where  $T_0$  and  $\Sigma_0$  are the temperature and surface density at an arbitrary radius  $r_0$ . The opacity law is also assumed to be a power law following Beckwith & Sargent (1991), as shown in Eq. 3. Therefore, the optical depth at a given wavelength (frequency) and radius can be written as:

$$\tau_\nu(r) = \Sigma_0 \kappa_0 \left( \frac{r}{r_0} \right)^{-p} \left( \frac{\nu}{230 \text{ GHz}} \right)^\beta \quad (8)$$

Here,  $\kappa_0$  is the opacity value at 230 GHz (we consider 230 GHz instead of 1000 GHz as in Eq. 3, due to the common use of 1.3 mm as the reference wavelength). However,  $\kappa_0$  also depends on the maximum grain size (e.g. D'Alessio et al. 2001), and it should not be left constant when modeling while changing  $\beta$  (this could introduce artificial trends in the modeling results, e.g. Ricci et al. 2010b). We therefore combined  $\Sigma_0$  and  $\kappa_0$  into  $\tau_{\nu, r_0}$ , i.e. the optical depth at the arbitrary radius  $r_0$  (set to 10 au in our study) and at 230 GHz:

$$\tau_\nu(r) = \tau_{1.3 \text{ mm}, 10 \text{ AU}} \left( \frac{r}{10 \text{ AU}} \right)^{-p} \left( \frac{\nu}{230 \text{ GHz}} \right)^\beta \quad (9)$$

With this setup, there are a total number of eight free parameters in this model:  $\tau_{1.3 \text{ mm}, 10 \text{ au}}$ ,  $r_{in}$ ,  $R_d$ ,  $T_{10 \text{ au}}$ ,  $p$ ,  $q$ ,  $i$ , and  $\beta$ . Because we will model far-IR and (sub)mm fluxes, the inner radius does not have a crucial effect in our modeling and was fixed to 0.01 au following Andrews & Williams (2005) - a rough estimate of where dust sublimation occurs (Dullemond et al. 2001; Muzerolle et al. 2003). Therefore, seven free parameters remain.

Spectral indices  $\alpha \sim 2$  can be produced both by compact, optically thick disks (small  $R_d$ , typically  $< 50$  au, high  $\tau_{1.3 \text{ mm}, 10 \text{ au}}$ , and unconstrained  $\beta$ ), or bigger, optically thin disks with large dust grains (larger and unconstrained  $R_d$ , low  $\tau_{1.3 \text{ mm}, 10 \text{ au}}$  and  $\beta$  values). As a result,  $\tau_{1.3 \text{ mm}, 10 \text{ au}}$ ,  $R_d$ , and  $\beta$  estimates become degenerate in these cases from SED fitting alone. Observationally, most resolved disks have been found to extend for about (or more than) 50-150 au (Andrews et al. 2010; Ricci et al. 2010a,b, 2014), but the difficulty in resolving smaller and usually fainter disks introduces an important bias. Recent high-resolution observations have identified a population of small disks (e.g. Piétu et al. 2014; Osorio et al. 2016; Testi et al. 2016), and consequently they cannot be ruled out in the analysis. In an effort to break this degeneracy, we gathered disk radii

from Andrews & Williams (2007), Ricci et al. (2010a,b), Piétu et al. (2014), and Pascucci et al. (2016). In the last case, disk radii were estimated from FWHM measurements converted to physical sizes using the distance to Chamaeleon I, and uncertainties of 25% were assigned.

For each source, we aim at fitting data between 70  $\mu\text{m}$  and 5 mm. We also included the processed SPIRE spectra (when available) after binning them in five points to avoid giving them excessive weight, by simply dividing the corresponding wavelength range in five equal sub-ranges, and adopting the median flux value in each of them. For consistency with our previous *Herschel* data processing, we assigned 20% uncertainties to these data. Inspection of uncertainties of the ancillary data revealed that many of them were underestimated, probably due to a lack of the systematic contribution. We circumvented the issue by assigning 20% uncertainties to measurements with smaller values. We note that the effect of this is to produce more conservative uncertainties in our final estimates, and it should not affect our results. We adopted a Bayesian methodology and used the *ensemble samplers with affine invariance* (Goodman & Weare 2010) variation of the Markov Chain Monte Carlo (MCMC) method via the *emcee* software (Foreman-Mackey et al. 2013). Priors were chosen based on the interest of each parameter and typical values in previous studies:

1.  $R_d$ : if the source had information about its radius from Andrews & Williams (2007), Ricci et al. (2010a), or Ricci et al. (2010b) where a range of values was quoted, a flat prior was assumed over the corresponding ranges. For resolved objects in Piétu et al. (2014) or Pascucci et al. (2016), a Gaussian prior was used centered at the reported disk radii, with a standard deviation equal to the corresponding uncertainty. For objects with no resolved information, a flat prior from 10 to 300 au was assumed.
2.  $\tau_{1.3 \text{ mm}, 10 \text{ AU}}$ : flat prior from  $10^{-3}$  to  $10^3$ , considering extreme values of  $\kappa_{1.3 \text{ mm}}$  and  $\Sigma_{10 \text{ au}}$ . Because the range extends for several orders of magnitude, this parameter was explored in logarithmic scale.
3.  $T_{10 \text{ AU}}$ : flat prior from 5 to 500 K.
4.  $p$ : flat prior from 0.5 to 1.5. This covers fiducial values used in modeling (e.g. Andrews & Williams 2005).
5.  $q$ : Gaussian prior centered at 0.5 with a standard deviation of 0.1. This accounts for the typical spread obtained in models (e.g. Chiang & Goldreich 1997; D'Alessio et al. 1998).



6.  $i$ : inclination values larger than 80 degrees were excluded to avoid issues at very high inclinations. For the remaining inclinations, a geometric prior  $\sin(i)$  was used.

7.  $\beta$ : flat prior from 0 to 2.5, based on  $\beta$  measurements of disks (Ricci et al. 2010a,b; Ubach et al. 2012).

As already mentioned, the considered models have seven free parameters. In the adopted approach, the use of restrictive priors for some of them (e.g.  $p$ ,  $q$ , inclination) provides additional information to the fitting process. We chose to model objects with data available for at least seven different wavelengths, combining photometry and the binned SPIRE spectra. We also required the minimum wavelength available to be smaller than  $200 \mu\text{m}$  and the maximum one to be above  $800 \mu\text{m}$  to guarantee a reasonable coverage of the far-IR/mm part of the SEDs. Sixty-three objects in the sample meet this criterion: 40 in Taurus, 5 in Ophiuchus, and 14 in Chamaeleon I. From these, 28 had some information about their disk radii from resolved high-resolution observations. In the *emcee* setup for each source, 40,000 iterations with 50 walkers were run, and the last 10,000 steps were used to generate our posterior distributions. The chains were visually inspected for convergence, and we also checked that the adopted burn-in range (the discarded initial 30,000 steps) was at least five times the corresponding autocorrelation time.

The adopted procedure yielded satisfactory fits in all cases, and the obtained posterior functions revealed that  $\tau_{1.3\text{mm},10\text{au}}$ ,  $T_{10\text{au}}$ , and  $\beta$  are generally constrained to some extent. As expected, the posteriors of  $p$ ,  $q$ , and  $i$  follow the assumed priors because they are largely unconstrained with SEDs alone. Despite our efforts to include resolved information, some objects displayed a bi-modal behavior in their  $R_d$ ,  $\tau_{1.3\text{mm},10\text{au}}$ , and  $\beta$  posteriors, as corresponds to the degenerate case formerly mentioned. Although the distributions for  $T_{10\text{au}}$  are still informative (the Bayesian methodology naturally accounts for the existence of degeneracies), the bi-modal posteriors of  $\tau_{1.3\text{mm},10\text{au}}$  makes them complex to analyze, and we excluded these objects when focusing on these parameters in particular. The obtained results for  $\tau_{1.3\text{mm},10\text{au}}$ ,  $T_{10\text{au}}$ , and  $\beta$  are reported in Table 7. An example of a well-behaved source (DL Tau) is shown in Fig. 6.

**Table 7.** Modeling Results (Median, 16th, and 84th percentiles).

Name	$\tau_{1.3\text{mm},10\text{AU}}$	$\beta$	$T_{10\text{AU}}$ [K]
AA Tau <sup>†</sup>	$-0.6^{+0.5}_{-0.3}$	$0.9^{+0.3}_{-0.3}$	$43^{+6}_{-8}$
AB Aur	$-1.1^{+0.3}_{-0.2}$	$1.4^{+0.1}_{-0.2}$	$178^{+35}_{-51}$
BP Tau	$-0.3^{+0.3}_{-0.3}$	$1.4^{+0.3}_{-0.4}$	$31^{+5}_{-7}$
CIDA 7	$-0.8^{+0.5}_{-2.6*}$	$0.7^{+0.5}_{-0.9*}$	$34^{+6}_{-7}$
CIDA 9	$-0.3^{+0.6}_{-2.0*}$	$0.9^{+0.6}_{-0.9*}$	$35^{+5}_{-6}$
CI Tau <sup>†</sup>	$-0.2^{+0.3}_{-0.2}$	$1.3^{+0.3}_{-0.4}$	$47^{+6}_{-10}$
CW Tau <sup>†</sup>	$-0.0^{+0.2}_{-0.2}$	$1.9^{+0.6}_{-0.4}$	$58^{+6}_{-5}$
CY Tau <sup>†</sup>	$0.1^{+0.4}_{-0.3}$	$0.7^{+0.4}_{-0.4}$	$25^{+3}_{-5}$
DD Tau	$-1.4^{+0.6}_{-1.9}$	$0.3^{+0.2}_{-0.6}$	$66^{+16}_{-49}$
DE Tau <sup>†</sup>	$0.5^{+0.4}_{-1.6*}$	$1.5^{+0.9}_{-0.7*}$	$53^{+8}_{-7}$
DG Tau	$0.1^{+0.4}_{-0.4}$	$0.7^{+0.2}_{-0.4}$	$94^{+13}_{-20}$
DH Tau	$0.4^{+1.5}_{-1.7*}$	$0.5^{+0.4}_{-1.1*}$	$37^{+6}_{-8}$
DK Tau	$0.6^{+1.9}_{-1.7*}$	$0.5^{+0.3}_{-1.1*}$	$50^{+9}_{-20}$
DL Tau <sup>†</sup>	$0.0^{+0.3}_{-0.3}$	$1.0^{+0.2}_{-0.2}$	$42^{+4}_{-8}$
DN Tau <sup>†</sup>	$-0.3^{+0.3}_{-0.3}$	$0.6^{+0.3}_{-0.4}$	$36^{+5}_{-7}$
DO Tau <sup>†</sup>	$-0.6^{+0.3}_{-0.3}$	$0.3^{+0.1}_{-0.1}$	$78^{+11}_{-14}$
DQ Tau	$0.1^{+0.4}_{-0.3*}$	$1.8^{+0.7}_{-0.4*}$	$38^{+7}_{-10}$
DS Tau	$-0.7^{+0.5}_{-1.4*}$	$0.6^{+0.4}_{-0.7*}$	$29^{+5}_{-6}$
FM Tau <sup>†</sup>	$1.5^{+1.1}_{-1.0*}$	$1.1^{+0.8}_{-0.9*}$	$34^{+6}_{-6}$
FN Tau	$-1.5^{+0.6}_{-2.0}$	$0.2^{+0.1}_{-0.5}$	$85^{+25}_{-66}$
FT Tau <sup>†</sup>	$-0.4^{+0.8}_{-1.9}$	$0.5^{+0.3}_{-0.6}$	$43^{+6}_{-11}$
FV Tau	$-1.6^{+0.5}_{-0.3*}$	$1.0^{+0.5}_{-0.6*}$	$57^{+13}_{-42}$
GM Aur <sup>†</sup>	$-0.3^{+0.4}_{-0.3}$	$1.5^{+0.2}_{-0.2}$	$54^{+6}_{-10}$
GO Tau <sup>†</sup>	$-0.3^{+0.3}_{-0.2}$	$1.5^{+0.2}_{-0.3}$	$30^{+3}_{-5}$
Haro 6-13	$-0.5^{+0.4}_{-0.3}$	$0.6^{+0.2}_{-0.2}$	$78^{+11}_{-15}$
HK Tau	$-0.9^{+0.3}_{-0.3}$	$0.9^{+0.2}_{-0.2}$	$55^{+7}_{-10}$
IRAS 04125+2902	$-1.1^{+0.4}_{-0.4}$	$1.0^{+0.4}_{-0.5}$	$47^{+8}_{-10}$
IRAS 04385+2550	$-1.0^{+0.5}_{-0.3}$	$0.6^{+0.1}_{-0.2}$	$66^{+10}_{-16}$
IP Tau	$-0.9^{+0.6}_{-0.2*}$	$1.7^{+1.2}_{-0.5*}$	$24^{+5}_{-16*}$
IQ Tau <sup>†</sup>	$-0.4^{+0.3}_{-0.3}$	$0.8^{+0.3}_{-0.3}$	$37^{+5}_{-7}$
LkCa 15	$-0.0^{+0.3}_{-0.3}$	$1.4^{+0.2}_{-0.3}$	$42^{+4}_{-8}$
RW Aur	$-1.2^{+0.7}_{-3.1*}$	$0.1^{+0.1}_{-1.4*}$	$91^{+23}_{-80}$
RY Tau	$-0.3^{+0.5}_{-0.5}$	$0.6^{+0.2}_{-0.6}$	$92^{+13}_{-19}$
UX Tau A+C	$-0.7^{+0.4}_{-0.3}$	$0.8^{+0.3}_{-0.4}$	$59^{+8}_{-12}$
UY Aur	$-1.3^{+0.4}_{-0.3}$	$0.9^{+0.2}_{-0.2}$	$78^{+13}_{-18}$
UZ Tau A <sup>†</sup>	$-0.3^{+0.4}_{-0.3}$	$0.7^{+0.3}_{-0.3}$	$48^{+6}_{-10}$
V710 Tau	$-0.4^{+0.3}_{-0.2*}$	$1.7^{+0.5}_{-0.6*}$	$30^{+3}_{-5}$
V807 Tau	$-1.6^{+0.5}_{-0.5}$	$0.6^{+0.4}_{-0.5}$	$51^{+13}_{-32}$
V836 Tau <sup>†</sup>	$-0.2^{+0.3}_{-0.7}$	$0.5^{+0.3}_{-1.1}$	$34^{+6}_{-5}$
V892 Tau	$-0.6^{+0.4}_{-0.3}$	$0.6^{+0.1}_{-0.2}$	$153^{+28}_{-44}$
ZZ Tau IRS	$-0.3^{+0.3}_{-0.2}$	$2.2^{+0.4}_{-0.2}$	$54^{+7}_{-12}$
DOAR16AB	$-1.1^{+0.5}_{-1.7*}$	$0.6^{+0.4}_{-0.8*}$	$53^{+10}_{-23}$

Table 7 continued

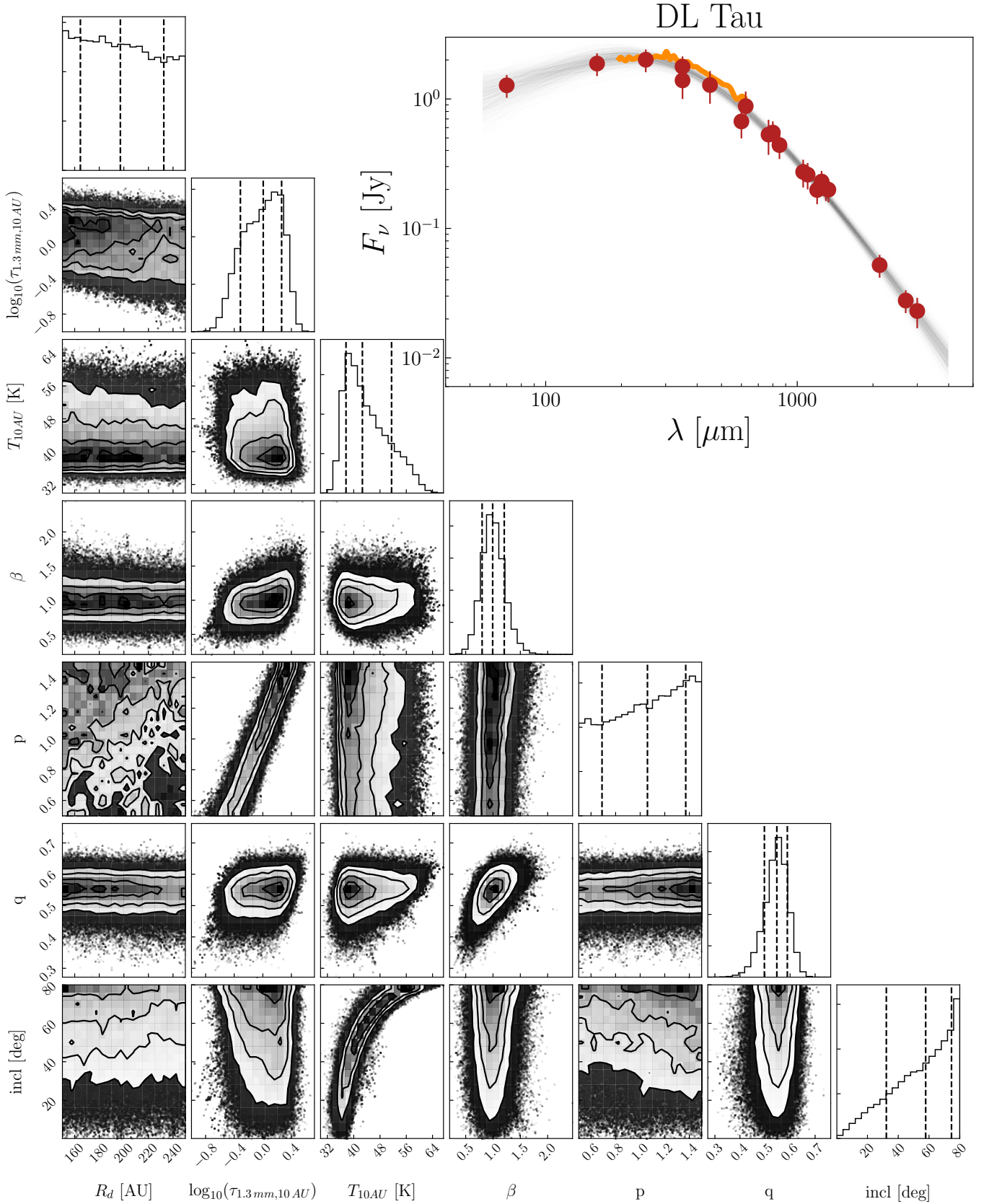


**Figure 6.** Fitting results for DL Tau. The corner plot shows the posterior distributions for parameters and the corresponding 2D projections. Vertical dashed lines show the 16th, 50th, and 84th percentiles. The inset shows the fitted photometry (red circles) and SPIRE spectrum (yellow line), together with 1000 models randomly selected from the posterior distributions (dark area). This object is a well-behaved case for which  $\tau_{1.3\text{mm},10\text{AU}}$ ,  $T_{10\text{AU}}$ , and  $\beta$  do not become degenerate.

Table 7 (*continued*)

Name	$\tau_{1.3\text{ mm},10\text{ AU}}$	$\beta$	$T_{10\text{ AU}}$ [K]
DOAR25 <sup>†</sup>	$-0.1^{+0.3}_{-0.3}$	$0.6^{+0.2}_{-0.2}$	$49^{+5}_{-7}$
GSS39	$0.4^{+0.4}_{-0.4}$	$0.9^{+0.3}_{-0.4}$	$39^{+5}_{-8}$
SR21AB <sup>†</sup>	$-1.3^{+0.4}_{-0.3}$	$1.4^{+0.1}_{-0.2}$	$106^{+14}_{-22}$
IRS48	$-1.4^{+0.4}_{-0.3}$	$0.7^{+0.2}_{-0.3}$	$236^{+73}_{-133}$
IRS49	$-0.9^{+0.8}_{-2.8}$ *	$0.3^{+0.2}_{-1.1}$ *	$65^{+13}_{-41}$
WSB60 <sup>†</sup>	$-0.6^{+0.6}_{-0.4}$	$0.6^{+0.3}_{-0.3}$	$44^{+7}_{-8}$
ROX-44 <sup>†</sup>	$-1.1^{+0.4}_{-0.4}$	$0.1^{+0.1}_{-0.2}$	$97^{+25}_{-41}$
SX Cha	$-1.2^{+0.5}_{-0.8}$	$0.4^{+0.3}_{-0.5}$	$50^{+12}_{-29}$
SZ Cha	$-0.2^{+0.3}_{-0.2}$	$1.8^{+0.3}_{-0.4}$	$62^{+8}_{-13}$
TW Cha <sup>†</sup>	$-0.2^{+0.4}_{-1.9}$ *	$0.5^{+0.4}_{-1.1}$ *	$35^{+6}_{-5}$
CR Cha <sup>†</sup>	$0.1^{+0.2}_{-0.2}$	$2.2^{+0.3}_{-0.2}$	$52^{+6}_{-7}$
CS Cha <sup>†</sup>	$0.1^{+0.4}_{-0.3}$ *	$1.6^{+0.9}_{-0.7}$ *	$67^{+11}_{-9}$
CT Cha	$-0.0^{+0.6}_{-2.1}$ *	$0.7^{+0.5}_{-1.1}$ *	$41^{+6}_{-7}$
CU Cha	$-0.2^{+0.3}_{-0.3}$	$2.3^{+0.3}_{-0.2}$	$156^{+29}_{-39}$
T33A <sup>†</sup>	$-0.5^{+0.3}_{-0.4}$ *	$1.1^{+0.3}_{-1.1}$ *	$83^{+15}_{-19}$
VZ Cha	$0.2^{+0.6}_{-1.7}$ *	$1.1^{+0.8}_{-0.9}$ *	$31^{+4}_{-7}$
B43	$0.9^{+1.0}_{-1.4}$ *	$1.0^{+0.7}_{-1.0}$ *	$26^{+3}_{-4}$
T42 <sup>†</sup>	$-1.3^{+0.2}_{-0.2}$	$2.1^{+0.3}_{-0.3}$	$88^{+11}_{-18}$
WW Cha <sup>†</sup>	$0.2^{+0.3}_{-0.2}$	$1.8^{+0.5}_{-0.5}$	$99^{+12}_{-15}$
T47 <sup>†</sup>	$-0.6^{+0.3}_{-1.5}$	$0.3^{+0.2}_{-0.8}$	$41^{+7}_{-7}$
CV Cha <sup>†</sup>	$0.3^{+1.0}_{-1.9}$ *	$1.0^{+0.7}_{-1.0}$ *	$80^{+15}_{-15}$
T56 <sup>†</sup>	$-0.7^{+0.3}_{-1.4}$ *	$0.6^{+0.4}_{-1.1}$ *	$46^{+8}_{-7}$

**Notes.**

<sup>†</sup> Object with  $R_d$  constraints from resolved observations.

\* Unconstrained/bimodal distribution.

Before analyzing these results, it is important to mention that the disk model used here is a very simplistic approximation. It assumes a fixed inner radius and an axisymmetric geometry. More importantly, it does not include a vertical temperature gradient or dust mixing/settling, which produce flared disks required to properly explain far-IR fluxes of disks (e.g. [Kenyon & Hartmann 1987](#); [Calvet et al. 1992](#)). We have also assumed a power-law opacity law longward of  $\sim 70\ \mu\text{m}$ , which is not realistic in the presence of different dust species (e.g. [D’Alessio et al. 2001](#); [Draine 2006](#)). These two last issues combined are especially relevant for  $\beta$  estimates, which may therefore be higher than the expected  $\alpha = 2 + \beta$  relation. Thus, although they can provide interesting insights and comparisons, the results from the modeling should therefore be considered with caution.

4.1. *Optical depth and  $\beta$  values*

Despite having included disk size estimates from the literature, some objects lacked that information, or the measured size ranges were not restrictive enough to avoid the degeneracy in the fitting process. Here, we limit our analysis to non-degenerate  $\tau_{1.3\text{ mm},10\text{ au}}$  and  $\beta$  distributions, as revealed by their well-behaved distributions (i.e. constrained and not bi-modal). Therefore, 40 objects were used to study these parameters, 28 in Taurus, 6 in Ophiuchus, and 6 in Chamaeleon I.

The ensemble distributions of  $\tau_{1.3\text{ mm},10\text{ au}}$ , and  $\beta$  for each region (produced by randomly selecting 1 million positions from the individual posteriors) are shown in the top and middle panels in Fig. 7<sup>3</sup>. We first note that the low number of sources remaining after the adopted curation processes both in Ophiuchus and Chamaeleon I is an obvious caveat to our interpretation, and therefore it cannot be extrapolated to the whole sample. However, they can still be used to investigate possible differences among regions, under the assumption that these distributions are not very different from the underlying ones (or at least that they are different in similar ways). In the following, we assume this to be the case, bearing in mind that additional observations may improve and modify some of these results.

The distribution of optical depth values at 10 au and 1.3mm (Fig. 7, top) has its maximum at  $\log \tau_{1.3\text{ mm},10\text{ au}} = -0.25$  (corresponding to  $\tau_{1.3\text{ mm},10\text{ au}} \sim 0.5$ ), and a secondary peak at  $\log \tau_{1.3\text{ mm},10\text{ au}} = -1$ . We note that the shape of this distribution is determined mostly by Taurus, given the lack of sufficient long-wavelength data for most objects in Chamaeleon I and Ophiuchus, and the distributions in these regions appear to be broader than the one in Taurus (again, this interpretation is limited by the small number statistics in these regions). For comparison, reasonable assumptions about the dust opacity and surface density based on observations of the solar system bodies yield  $\tau_{1\text{ mm}}=1$  at  $\sim 10\text{ au}$  for the Minimum Mass Solar Nebula ([Davis 2005](#)), suggesting that several of the modeled protoplanetary disks may have optical depth profiles (and hence possibly surface densities) similar to that of the parental disk of the solar system. In the case of  $\beta$ , values smaller than the one measured for the ISM ( $\sim 1.6-2$ ; see e.g. [Draine 2006](#), and references therein) imply some degree of grain growth. Almost the entirety of the Taurus and Ophiuchus distributions (and part of Chamaeleon I) are constrained within that value, in correspondence with the observational result

<sup>3</sup> Given the large number of MCMC steps and the computational requirement to compute KDEs in these particular cases, we displayed these distributions using histograms with a large (100) number of bins.

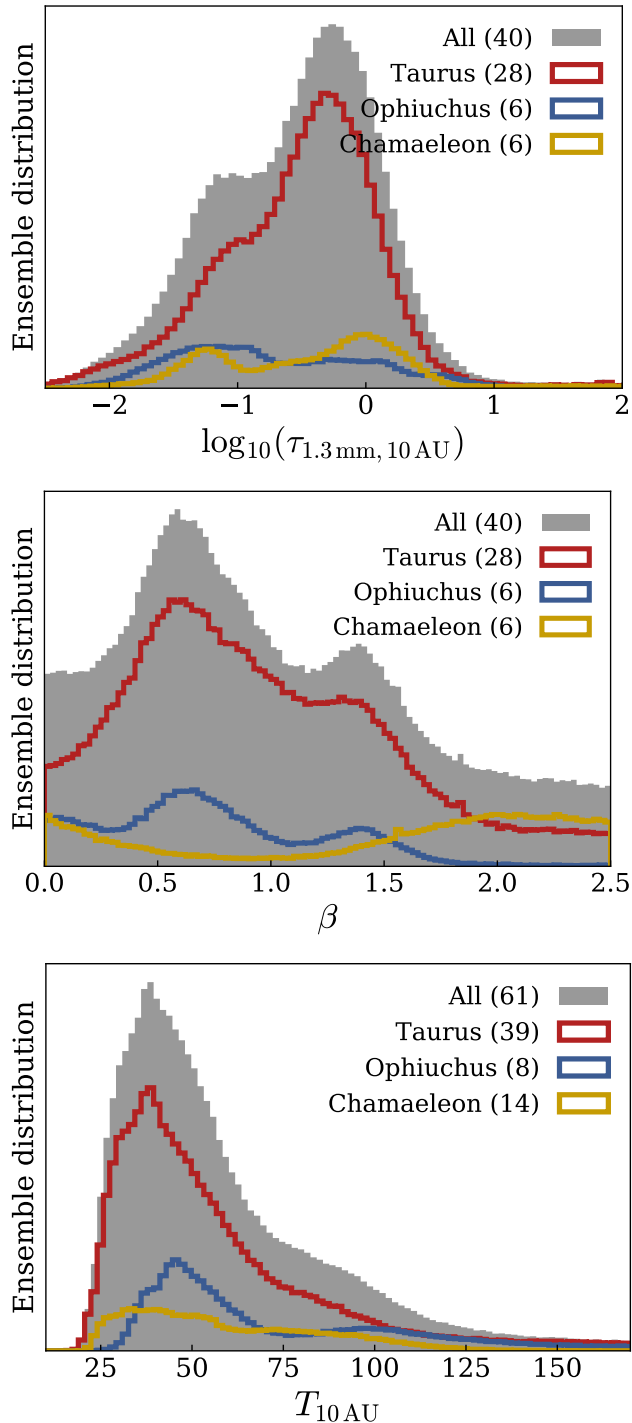


**Figure 7.** Ensemble distributions for  $\tau_{1.3\text{mm}, 10\text{au}}$  (top),  $\beta$  (middle), and  $T_{10\text{AU}}$  (bottom) for each region, normalized to the number of objects in each association. Sources with bi-modal (degenerate) and flat (uninformative) distributions have been excluded. The number of objects in each case is indicated in the legend.

discussed in Sec. 3.3. As with  $\alpha_{\text{mm}}$ , Chamaeleon I shows a different behavior (an excess of high  $\beta$  values) that will be discussed further on. We note that the distributions of  $\beta$  should be considered with caution, not only due to the aforementioned caveats, but also because degenerate cases have been removed from the analysis. Because these occur when  $\alpha = 2$ , this procedure inevitably discards objects with  $\beta \sim 0$ . There is a tentative bimodality in both distributions, and especially in the case of  $\beta$ , with a tentative secondary peak occurring at  $\sim 1.4$ - $1.5$ . Given the limited size of the modeled sample and the simplicity of the models used, we do not investigate this issue in detail here. However, we speculate that, if real, it may hint at a quick transition from micron-sized grains (large  $\beta$  values) to mm/cm-sized dust (smaller  $\beta$ ).

We also inspected our results in the  $\tau_{1.3\text{mm}, 10\text{au}}$  versus  $\beta$  space. Individually, these two parameters affect the optical depth—and are therefore correlated—but a more general correlation may also exist as a result of disk evolution. Fig. 8 shows that objects with low  $\beta$  values ( $\lesssim 1$ ) spread through optical depth values from  $\log_{10}(\tau_{1.3\text{mm}, 10\text{au}}) = -1.5$  to  $0.5$ . However, a lack of low optical depths is found for  $\beta$ s above that threshold, an expected effect from an observational bias toward bright sources: mm fluxes decrease faster with increasing wavelengths for steeper  $\beta$  values, and only massive disks (likely to be optically thicker) are detectable. Although such an effect could also be partially produced by disk evolution (disk masses decrease with time, and dust growth leads to smaller  $\beta$ s), more complex models are required to quantify how much (if any) of this paucity of low  $\beta$  - low optical depth values is due to disk evolution itself. Like Fig. 5, Fig. 8 also shows the position of (pre)transitional disks (as classified in Sec. 3.4), with no obvious difference between these sources and full disks.

#### 4.2. Disk temperatures at 10 au

The modeling process also yielded estimates of the disk temperature at 10 au. For this parameter—even when the disk radii, optical depth, and  $\beta$  are degenerate—the posterior  $T_{10\text{au}}$  is constrained to some extent, in most cases. Only two of the modeled sources displayed an uninformative ( $\sim$  flat) posterior distribution and were excluded from the analysis, leaving 39 objects in Taurus, 8 in Ophiuchus, and 14 in Chamaeleon I. Fig. 7 (bottom) shows the results for the three regions, all of them showing a distribution that peaks at  $\sim 40$ - $50$  K with a lower probability tail extending to  $\sim 100$ - $150$  K due to the effect of high inclinations (see corner plot in Fig. 6).

The obtained  $T_{10\text{au}}$  values can be used to test the general performance of these models by comparing them with the luminosity of their host star: despite the former

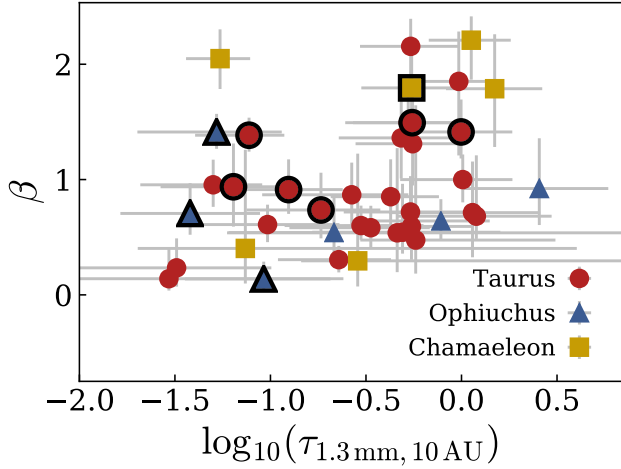


**Figure 8.**  $\beta$  vs. optical depths at 1.3 mm and 10 au for Taurus (red), Ophiuchus (blue), and Chamaeleon (yellow) objects. Symbols with black borders are transitional disks.

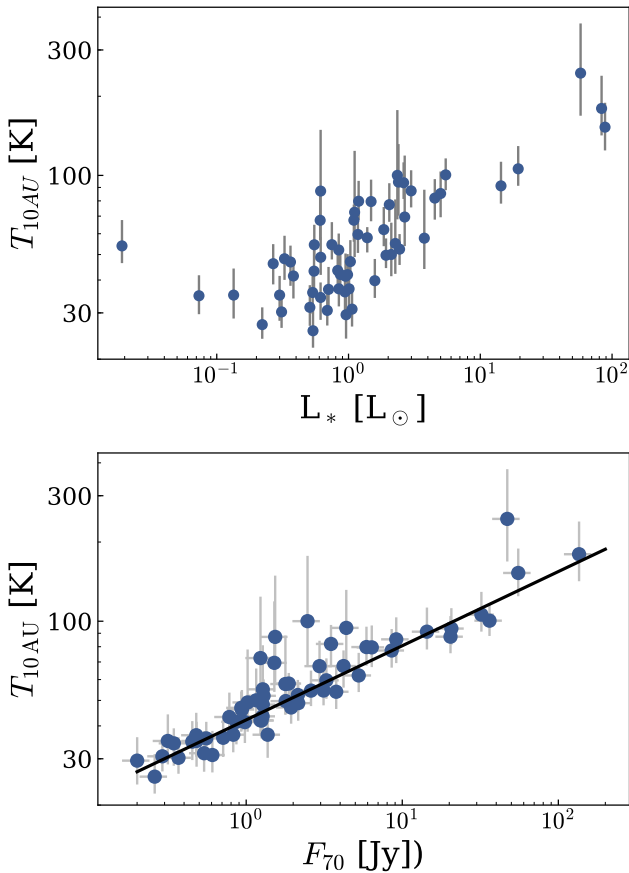


**Figure 9.** Top: stellar luminosities vs disk temperatures at 10 au as determined by the models. Bottom: Observed  $70 \mu\text{m}$  fluxes (scaled to 140 pc in the case of Chamaeleon I) vs. disk temperatures at 10 au as derived from the models. The relation derived in Eq. 10 is also shown as a black solid line.

parameter not being part of the adopted model, a clear correlation among these two is found (Fig. 9, top panel), showing that the obtained disk temperatures are higher for more luminous stars, as expected.

The temperature of the disk at 10 au is also related to far-IR fluxes; they trace both areas from which most of this emission originates, and wavelengths at which the deviation from the RJ regime is significant and provides information on the temperature of the region. Figure 9 shows the observed fluxes at  $70 \mu\text{m}$  with respect to the corresponding  $T_{10 \text{ AU}}$ , with an obvious correlation between these two parameters. The best fit for this trend yields:

$$\log_{10}(T_{10 \text{ au}}[\text{K}]) = (0.28 \pm 0.01) \log_{10}(F_{70}[\text{Jy}]) + (1.625 \pm 0.005) \quad (10)$$

We note that this tight relation is likely produced by the simplicity of model used: far-IR (mostly PACS) fluxes determine the value of  $T_{10 \text{ AU}}$  to a great extent. Such a close correlation is unlikely when considering more complex models with vertical temperature gradients and dust mixing (e.g. D’Alessio et al. 1998, 2006), which would introduce significant scatter in the  $70 \mu\text{m}$  fluxes. Nevertheless, this relation provides a rough estimate of the disk temperature at a few astronomical units from the star using far-IR observations, and it could have applications for comparative studies of disk samples.

#### 4.3. The peculiar case of Chamaeleon I

As mentioned in previous sections, Chamaeleon I shows a different behavior than Taurus and Ophiuchus; the spectral indices in its sources appear to be systematically larger with respect to the other regions. We applied both the Kolmogorov-Smirnov (KS) and Anderson-Darling (AD) tests to the estimated millimeter indices and found no significant differences between Taurus and Ophiuchus, while Chamaeleon I showed clear indications of a different distribution ( $p$ -values  $\sim 0.005$  and  $< 0.01$  for the KS and AD tests, respectively). This was already mentioned in Testi et al. (2014) based on the results of Ubach et al. (2012), who measured  $\alpha_{\text{mm}}=2.9\text{-}3.8$  for eight sources in this association. Assuming that the relation  $\beta = \alpha - 2$  can be used for these objects, the corresponding  $\beta$  values (0.9-1.8) hint at different dust properties of sources in these regions. Although this may be simply a result of the small number of sources with mm spectral index estimates in the region, here we discuss some of the plausible explanations for this phenomenon provided it is real.

Our results are in agreement with the aforementioned findings: after applying the various data curation processes,  $\alpha_{\text{mm}}$  values were measured for seven disks in Chamaeleon I. Out of these seven, four (CR Cha,



SZ Cha, WW Cha, and T33 A) have values larger than  $\alpha > 3$  (and the number would go up to five if we were to include the  $\alpha$  value for CU Cha in [van der Plas et al. 2017](#)). This represents 55-60% of the sample with available spectral index estimates in this region. For comparison, the fractions of objects with  $\alpha > 3$  in Taurus and Ophiuchus are 2% (1/58) and 9% (1/11), respectively. A similar (but more uncertain) result is found when analyzing the  $\beta$  distributions from the models, where Chamaeleon I shows an excess of high values ( $> 1.5$ ). Although an in-depth analysis of each data set would be required to completely rule out systematic problems in any of the sources of ancillary (sub)mm data used for Chamaeleon I, our inspection of the corresponding SEDs revealed no apparent issue—and this result is still present when using individual studies to estimate spectral indices. We therefore discard the possibility of this being a data-processing problem.

Chamaeleon I is estimated to be the oldest region of the considered sample, and hence its steeper (sub)mm slopes could be the result of dust evolution in its disks. These mm spectral indices imply high  $\beta$  values, suggestive of a decrease in the maximum grain size in the outer regions of these disks. Such a trend is expected from the inward drift of mm/cm-sized grains in the presence of gas: at these sizes, dust particles start experiencing a head wind from the gas, losing angular momentum and spiraling inward ([Adachi et al. 1976](#); [Weiden-schilling 1977](#); [Takeuchi & Lin 2002](#)). This mechanism clears out the outer regions of the disk of mm/cm-sized grains (if they are not replenished by other means) and effectively decreases the value of  $a_{max}$ , thus increasing  $\beta$  as a function of radius (e.g. [Birnstiel et al. 2010](#); [Pinilla et al. 2012](#)). Disk lifetimes are on the order of 5-10 Myr ([Haisch et al. 2001](#); [Hernández et al. 2007](#); [Ribas et al. 2015](#)), but the inward migration of mm/cm grains is estimated to be much faster ( $10^4$ - $10^5$  years, e.g. [Takeuchi & Lin 2005](#); [Brauer et al. 2007](#)); braking mechanisms, such as dust accumulation at pressure bumps, are required to slow down this inward migration (e.g. [Zhu et al. 2011](#); [Pinilla et al. 2012](#)) and explain observed mm spectral indices in disks ([Testi et al. 2014](#)). A possible explanation for the higher  $\alpha_{mm}$  values in Chamaeleon I is that dust migration has significantly altered disks in this region, but is still not as important in Taurus and Ophiuchus. However, Chamaeleon I sources with steep  $\beta$  values are also among the brightest objects at mm wavelengths in the sample (Fig. 5), in contradiction with the expected decline of disk masses with time (produced by viscous evolution and/or the decrease in mm opacities caused by inward migration of dust). If the fact that disks in Chamaeleon I are older was the only reason for differences in spectral indices, then these disks would have needed to be initially more massive than their counter-

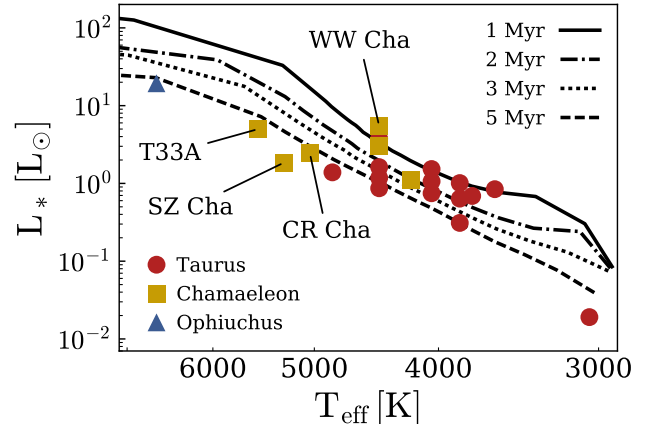


**Figure 10.** H-R diagram for sources with  $\alpha_{mm} > 2.5$  and  $T_*$  between 3000 and 7000 K. Objects in Taurus (red circles), Chamaeleon I (yellow squares), and Ophiuchus (blue triangles) are shown. [Siess et al. \(2000\)](#) isochrones are also shown for 1, 2, 3, and 5 Myr. The four labeled Chamaeleon I sources have  $\alpha_{mm} > 3$ ; three of these appear to be older than most of their Taurus counterparts.

parts in Taurus and Ophiuchus for them to have their current brightness.

A different explanation for the abnormal millimeter spectral indices in Chamaeleon I could be a strong selection bias toward its youngest members. Chamaeleon I is both further and older than the other regions, meaning that its disks are likely dimmer, on average, than those of Taurus and Ophiuchus. As a result, it is possible that only the brightest (and therefore probably youngest) population of its disks is detected, where grain growth may not have reached advanced stages. One example of this is WW Cha, which is surrounded by a substantial amount of extended emission in the *Herschel* maps and possibly a young source still embedded in its parental cloud. To test this idea, Fig. 10 shows the H-R diagram for objects with  $\alpha_{mm} > 2.5$ . Several of these sources have  $T_* > 4000$  K, and therefore we used isochrones from [Siess et al. \(2000\)](#), which cover this temperature range. However, the fact that three out of the four sources with  $\alpha_{mm} > 3$  in Chamaeleon I appear to be older than most of their Taurus counterparts implies that a hypothetical bias toward the youngest sources is probably not enough to explain the systematically larger  $\alpha_{mm}$  values observed in Chamaeleon.

Nevertheless, we remark here that the number of objects with available  $\alpha_{mm}$  measurements in Chamaeleon I is still small; although the recent ALMA survey by [Pascucci et al. \(2016\)](#) has yielded  $887 \mu\text{m}$  flux measurements for several sources in this region, measurements at longer wavelengths are still scarce. Therefore, these results should be considered with caution. Follow-up surveys in the mm will provide spectral slopes for several additional sources and determine whether the dif-

ference in spectral indices in Chamaeleon I is real or an observational/small-sample effect.

### 5. MEDIAN SEDS

Using the compiled data set, we produced and compared the median SEDs of Class II objects in each region. (Pre)transitional disks and Class III sources were first discarded using the procedure in [McClure et al. \(2010\)](#); Class II objects have  $-0.8 < \alpha_{5-12} < 1.25$  (in  $F_\nu$  versus  $\nu$  space). We required at least one detec-

tion at  $70\ \mu\text{m}$  or longer wavelengths for any source to be included, in order to mitigate different completeness levels at different wavelengths. A total of 114 objects met these criteria: 70 in Taurus, 26 in Chamaeleon, and 18 in Ophiuchus. The median SEDs, together with the 25th and 75th percentiles, were then computed using the dereddened SEDs after scaling each object to its 2MASS  $J$  flux. Only photometric bands with at least five measurements are available were included in the median SED calculation. The results are provided in Tables 8–9.

**Table 8.** Median SED, Upper, and Lower Quartiles of Taurus. SEDs are Normalized to the  $J$  Band

$\lambda$ [ $\mu\text{m}$ ]	$F_\nu$ , Percentile 25 %	$F_\nu$ , Median	$F_\nu$ , Percentile 75 %	N points	Reference
(1)	(2)	(3)	(4)	(5)	(6)
0.35	1.05e-02	2.59e-02	6.16e-02	19	a
0.36	3.42e-02	7.56e-02	1.74e-01	42	a
0.44	7.35e-02	1.83e-01	2.47e-01	42	a
0.48	2.95e-02	6.47e-02	1.63e-01	23	a
0.55	1.18e-01	2.29e-01	3.62e-01	51	a
0.62	9.22e-02	2.10e-01	3.29e-01	25	a
0.64	3.06e-01	4.88e-01	6.68e-01	43	a
0.76	2.53e-01	3.25e-01	5.35e-01	16	a
0.79	5.18e-01	6.48e-01	7.46e-01	37	a
0.91	5.28e-01	5.94e-01	7.66e-01	19	a
1.24	1.00e+00	1.00e+00	1.00e+00	67	a
1.66	1.12e+00	1.22e+00	1.40e+00	67	a
2.16	1.01e+00	1.15e+00	1.59e+00	67	a
3.35	6.39e-01	1.08e+00	1.70e+00	39	a
3.36	7.55e-01	1.05e+00	1.42e+00	24	a
3.55	6.80e-01	1.08e+00	1.59e+00	28	a
3.55	7.11e-01	9.78e-01	1.51e+00	63	a
4.49	6.43e-01	9.21e-01	1.65e+00	65	a
4.60	6.05e-01	9.61e-01	1.60e+00	63	a
5.7	5.18e-01	7.97e-01	1.58e+00	66	a
7.9	5.61e-01	8.60e-01	1.91e+00	65	a
9.0	7.76e-01	1.32e+00	2.73e+00	49	a
10.5	8.55e-01	1.11e+00	2.24e+00	13	a
11.6	5.73e-01	1.08e+00	2.00e+00	63	a
12.0	9.57e-01	1.94e+00	3.56e+00	31	a
18	1.19e+00	2.37e+00	4.07e+00	41	a
22	9.12e-01	1.75e+00	3.60e+00	63	a
24	7.60e-01	1.37e+00	3.17e+00	56	a
25	1.34e+00	3.29e+00	5.47e+00	30	a
70	1.20e+00	2.24e+00	3.87e+00	56	PACS 70 (this work)
100	8.73e-01	1.75e+00	3.36e+00	33	PACS 100 (this work)

Table 8 continued

Table 8 (*continued*)

$\lambda$ [ $\mu\text{m}$ ]	$F_\nu$ , Percentile 25 %	$F_\nu$ , Median	$F_\nu$ , Percentile 75 %	N points	Reference
(1)	(2)	(3)	(4)	(5)	(6)
160	1.00e+00	1.93e+00	3.86e+00	54	PACS 160 (this work)
250	9.33e-01	2.05e+00	4.25e+00	40	SPIRE 250 (this work)
350	1.49e+00	2.38e+00	3.70e+00	14	a
350	8.36e-01	1.63e+00	3.90e+00	35	SPIRE 350 (this work)
443	8.30e-01	1.29e+00	1.81e+00	13	a
450	1.29e+00	1.87e+00	2.71e+00	7	a
500	5.65e-01	1.21e+00	2.45e+00	30	SPIRE 500 (this work)
600	7.15e-01	8.97e-01	1.30e+00	6	a
624	7.60e-01	1.23e+00	2.16e+00	7	a
769	5.78e-01	8.46e-01	1.13e+00	13	a
800	3.42e-01	4.28e-01	6.26e-01	11	a
850	3.99e-01	6.40e-01	9.12e-01	6	a
869	6.80e-02	2.15e-01	4.53e-01	38	a
880	5.65e-02	1.36e-01	3.80e-01	17	a
1056	2.86e-01	3.93e-01	5.96e-01	15	a
1100	2.57e-01	2.70e-01	4.27e-01	6	a
1200	4.63e-02	1.67e-01	2.49e-01	10	a
1250	5.59e-02	1.82e-01	2.39e-01	27	a
1300	1.06e-01	1.87e-01	3.09e-01	18	a
1330	1.09e-01	2.56e-01	4.10e-01	14	a
1360	4.62e-02	6.91e-02	9.65e-02	7	PdBI1.36mm (Piétu et al. 2014)
2126	6.51e-02	7.64e-02	1.17e-01	5	a
2700	2.08e-02	3.60e-02	6.36e-02	17	a
2974	4.53e-03	7.50e-03	2.08e-02	5	a

NOTE—a: data from Andrews et al. (2013).

**Table 9.** Median SED, Upper, and Lower Quartiles of Chamaeleon. SEDs are Normalized to the  $J$  Band

$\lambda$ [ $\mu\text{m}$ ]	$F_\nu$ , Percentile 25 %	$F_\nu$ , Median	$F_\nu$ , Percentile 75 %	N points	Reference
(1)	(2)	(3)	(4)	(5)	(6)
0.44	1.04e-01	1.73e-01	2.29e-01	17	B Johnson (APASS)
0.48	1.37e-01	1.86e-01	2.80e-01	18	g SDSS (APASS)
0.55	1.75e-01	2.65e-01	4.25e-01	17	V Johnson (APASS)
0.62	3.38e-01	3.93e-01	6.58e-01	17	r SDSS (APASS)
0.76	3.40e-01	4.67e-01	7.05e-01	17	i SDSS (APASS)
1.24	1.00e+00	1.00e+00	1.00e+00	26	2MASS $J$
1.66	1.25e+00	1.28e+00	1.39e+00	25	2MASS $H$

Table 9 continued

Table 9 (*continued*)

$\lambda$ [ $\mu\text{m}$ ]	$F_\nu$ , Percentile 25 %	$F_\nu$ , Median	$F_\nu$ , Percentile 75 %	N points	Reference
(1)	(2)	(3)	(4)	(5)	(6)
2.16	1.19e+00	1.26e+00	1.54e+00	25	2MASS <i>K</i>
3.35	7.87e-01	1.02e+00	1.69e+00	17	<i>WISE 1</i>
3.55	7.35e-01	9.43e-01	1.52e+00	18	IRAC 1
4.49	7.12e-01	8.97e-01	2.02e+00	19	IRAC 2
4.60	7.79e-01	1.06e+00	1.67e+00	18	<i>WISE 2</i>
5.7	5.81e-01	7.60e-01	2.14e+00	22	IRAC 3
7.9	6.14e-01	8.91e-01	2.42e+00	24	IRAC 4
9.0	8.62e-01	1.31e+00	2.45e+00	22	AKARI 9
11.6	8.52e-01	1.20e+00	2.15e+00	21	<i>WISE 3</i>
18	1.17e+00	1.75e+00	2.96e+00	20	AKARI 18
22	1.25e+00	1.68e+00	2.33e+00	21	<i>WISE 4</i>
24	1.03e+00	1.42e+00	2.05e+00	21	MIPS 1
70	1.37e+00	2.29e+00	5.94e+00	19	PACS 70 (this work)
100	1.35e+00	2.10e+00	4.70e+00	25	PACS 100 (this work)
160	1.12e+00	2.12e+00	2.78e+00	12	PACS 160 (this work)
250	4.83e-01	1.65e+00	2.04e+00	8	SPIRE 250 (this work)
350	1.12e+00	1.20e+00	1.94e+00	6	SPIRE 350 (this work)
500	5.08e-01	7.55e-01	1.41e+00	6	SPIRE 500 (this work)
870	9.35e-02	1.78e-01	3.02e-01	6	LABOCA 870 (Belloche et al. 2011)
887	4.42e-02	1.05e-01	2.53e-01	25	ALMA 887 (Pascucci et al. 2016)

**Table 10.** Median SED, Upper, and Lower Quartiles of Ophiuchus. SEDs are Normalized to the *J* Band

$\lambda$ [ $\mu\text{m}$ ]	$F_\nu$ , Percentile 25 %	$F_\nu$ , Median	$F_\nu$ , Percentile 75 %	N points	Reference
(1)	(2)	(3)	(4)	(5)	(6)
0.44	7.59e-02	1.96e-01	2.21e-01	7	B Johnson (APASS)
0.48	1.12e-01	2.82e-01	3.12e-01	9	g SDSS (APASS)
0.55	1.50e-01	3.81e-01	4.18e-01	7	V Johnson (APASS)
0.62	2.58e-01	3.95e-01	4.83e-01	7	R CMC15
0.62	2.94e-01	5.12e-01	6.65e-01	9	r SDSS (APASS)
0.76	4.83e-01	5.68e-01	7.05e-01	8	i SDSS (APASS)
1.24	1.00e+00	1.00e+00	1.00e+00	18	2MASS <i>J</i>
1.66	1.11e+00	1.18e+00	1.22e+00	18	2MASS <i>H</i>
2.16	9.97e-01	1.07e+00	1.23e+00	18	2MASS <i>K</i>
3.35	6.80e-01	8.22e-01	1.01e+00	17	<i>WISE 1</i>
3.55	6.17e-01	8.07e-01	1.10e+00	14	IRAC 1
4.49	4.43e-01	6.68e-01	9.10e-01	16	IRAC 2
4.60	4.42e-01	6.99e-01	8.99e-01	17	<i>WISE 2</i>

*Table 10 continued*

Table 10 (*continued*)

$\lambda$ [ $\mu\text{m}$ ]	$F_\nu$ , Percentile 25 %	$F_\nu$ , Median	$F_\nu$ , Percentile 75 %	N points	Reference
(1)	(2)	(3)	(4)	(5)	(6)
5.7	3.70e-01	6.25e-01	7.60e-01	17	IRAC 3
7.9	4.62e-01	7.57e-01	9.44e-01	16	IRAC 4
9.0	7.86e-01	1.04e+00	1.44e+00	12	<i>AKARI</i> 9
11.6	5.04e-01	7.22e-01	1.15e+00	17	<i>WISE</i> 3
18	8.26e-01	1.15e+00	1.23e+00	7	<i>AKARI</i> 18
22	6.92e-01	1.22e+00	1.85e+00	16	<i>WISE</i> 4
24	7.98e-01	1.33e+00	1.73e+00	17	MIPS 1
70	4.39e-01	9.50e-01	2.83e+00	14	PACS 70 (this work)
100	6.68e-01	1.16e+00	2.93e+00	11	PACS 100 (this work)
160	7.65e-01	2.34e+00	2.58e+00	5	PACS 160 (this work)
250	2.86e-01	1.54e+00	3.11e+00	7	SPIRE 250 (this work)
850	6.09e-02	2.07e-01	9.00e-01	5	SCUBA 850 ( <a href="#">Andrews &amp; Williams 2007</a> )
1300	2.46e-02	4.31e-02	2.36e-01	7	SCUBA 1300 ( <a href="#">Andrews &amp; Williams 2007</a> )
3300	4.50e-03	1.06e-02	4.22e-02	6	ATCA 3.3 ( <a href="#">Ricci et al. 2010a</a> )

The obtained SEDs are shown in Fig. 11. We found them to be identical within the quartiles down to the (sub)mm regime. This comparison expands the result in [Furlan et al. \(2009\)](#), where the median IRS spectra of Taurus, Chamaeleon, and Ophiuchus were already found to be very similar. This is somewhat surprising, given that the three regions have different ages and more evolved disks are expected in Chamaeleon I than in Taurus and Ophiuchus. Additionally, the extent of the upper and lower quartiles also appear to be similar for the three regions, suggesting a similar spread in disk morphologies in the three regions. We speculate that the intrinsic scatter in disk morphologies, together with the selection of Class II disks formerly applied (which effectively includes disks with certain spectral indices only), may erase existing trends with age. Including objects classified as (pre)transitional disks does not change this result, but the median SEDs compiled here do not include Class III or diskless sources; thus, they represent the typical SED of disks in the regions more so than the median SED of all objects. We also note that our sample is not complete, and these median SEDs are biased toward bright objects. Despite this, the lack of differences between the estimated medians, combined with the similar median IRS spectra of these associations, suggest that either Class II disks have very similar structures/properties in different star-forming regions (at least to the extent traceable with SEDs), or the intrinsic variations in their morphologies are broad

enough to create a “typical protoplanetary disk” SED. High-resolution observations have often revealed complex structures in disks, such as multiple rings, spiral arms, or dust traps (e.g. [Muto et al. 2012](#); [van der Marel et al. 2013](#); [ALMA Partnership et al. 2015](#)), favoring the second explanation, but the number of objects per region is still significantly small, particularly in Ophiuchus and Chamaeleon. Future surveys of large samples of disks, especially in the (sub)mm regime, will produce more complete and sensitive median SEDs, which may reveal unseen region-to-region differences and shed some light on the “typical” median SED of protoplanetary disks. For comparison, in Fig. 11 we also include the median SED of K/M-type stars in the Upper Scorpius (Upper Sco) region from [Mathews et al. \(2013\)](#). The absolute age of this region is still under debate, but there is strong evidence for Upper Sco being older than Taurus, Chamaeleon I, and Ophiuchus (4–13 Myr, e.g. [Preibisch et al. 2002](#); [Pecaut et al. 2012](#); [Herczeg & Hillenbrand 2015](#)). Although the optical part of the SEDs cannot be directly compared due to the different treatment in [Mathews et al. \(2013\)](#), the median SED of Upper Sco shows a deficit of near/mid-IR excess with respect to the younger ones, indicating that disks in Upper Sco are more evolved (e.g. more settled). In the future, extending the median SED of disks in Upper Sco to longer wavelengths will enable one to search for evidence of dust growth signatures in such older regions.



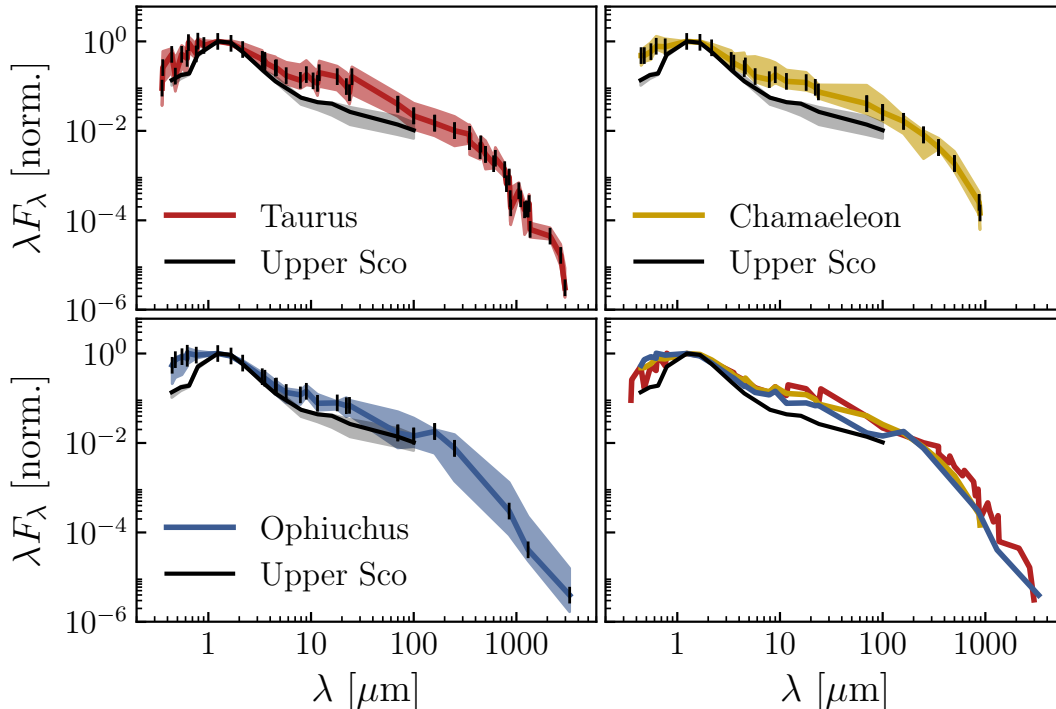


**Figure 11.** Obtained median SEDs for Taurus (top left), Chamaeleon (top right), and Ophiuchus (bottom left). These data sets are available as the Data behind the Figure. Shaded areas represent the first and third quartiles. The median SEDs are normalized to  $J$  band. Small black vertical lines mark the available wavelengths in each case. The bottom right panel compares the median SEDs of the three regions. The black line shows the median SED and quartiles of the older Upper Sco association from [Mathews et al. \(2013\)](#).

## 6. CONCLUSIONS

We have compiled multiwavelength data (including *Herschel* photometry and spectroscopy when available) for 284 Class II disks in the Taurus, Ophiuchus, and Chamaeleon I star-forming regions. These SEDs have been used to study different aspects of dust growth and properties of protoplanetary disks:

1. We investigated the spectral index of SEDs as a function of wavelength from the far-IR ( $70 \mu\text{m}$ ) to the millimeter, and determined that a small (5-20%) systematic shift is introduced in the calculation of the millimeter spectral index when combining SPIRE  $500 \mu\text{m}$  and (sub)mm observations.
2. We estimated millimeter spectral indices of disks in the three considered regions and found their values to be indicative of dust growth in disks in Taurus and Ophiuchus, in agreement with previous studies (e.g. [Lommen et al. 2007](#); [Ricci et al. 2010a,b](#); [Ubach et al. 2012](#)). In contrast, part of the disk population in Chamaeleon I seems to have smaller dust grains.
3. No correlations were found between the mm slopes and other tracers of disk evolution (near/mid-IR

spectral indices or properties of  $10 \mu\text{m}$  silicate feature). In particular, the dust properties of transitional disks show no appreciable difference with respect to full disks.

4. We used a Bayesian approach to fit the long wavelengths (longward of  $70 \mu\text{m}$ ) of sources with sufficient data, using a simple disk model. This allows us to estimate posterior distributions for the disk opacity at 10 au and 1.3 mm ( $\tau_{1.3\text{mm},10\text{au}}$ ), their temperature at the same distance ( $T_{10\text{au}}$ ), and the opacity-law exponent ( $\beta$ ). Disk radii from high-resolution observations were considered when possible to mitigate the degeneracy between compact, optically thick disks, and less dense disks with large ( $\gtrsim \text{mm}$ ) grains.
5. The optical depth values obtained are comparable to estimates for the Minimum Mass Solar Nebula. Given that large dust grains produce small  $\beta$  values, the obtained  $\beta$  values ( $< 1$ ) in most disks imply some dust growth with respect to the ISM. The individual analysis of the regions shows that, as already indicated by spectral indices, Chamaeleon contains disks with large  $\beta$  values.
6. The distribution of temperatures at 10 AU

( $T_{10\text{ AU}}$ ) peaks around 40-50 K and shows no significant difference among regions. A strong correlation of this parameter with observed  $70\ \mu\text{m}$  fluxes is also found.

7. There is evidence for a different distribution of spectral indices and  $\beta$ s in Taurus and Ophiuchus with respect to Chamaeleon I, the latter having steeper values. If this difference in spectral indices is caused by its older age, then the high millimeter fluxes of its disks require that they were initially more massive than their Taurus/Ophiuchus counterparts. After inspecting their location in the HR diagram, we find that a bias toward the youngest sources cannot explain all the steep slopes. Given the small number of sources with millimeter spectral index measurements in Chamaeleon I, this result should be confirmed with a larger sample.
8. We built the median SED of protoplanetary disks in each region and found them to be indistinguishable down to mm wavelengths within their quartiles, suggesting that either disks are quite similar in these associations or they display such a large variety of morphologies that produces a “typical” median SED.

Some of these results are tentative due to the small sample sizes, despite the large data compilation presented here. Future (sub)mm surveys of disks, especially in Ophiuchus and Chamaeleon I, will be critical to obtain better estimates of spectral indices at these wavelengths and, in particular, determine the origin of the apparently different spectral indices in Chamaeleon I. Additionally, analyzing the compiled data with detailed disk models such as the ones presented in [D’Alessio et al. \(1998, 1999, 2001, 2006\)](#), especially when combined with a Bayesian approach, will inform us of important processes such as the dust settling.

We thank the referee for their thorough review and comments that helped improve the quality of this manuscript. We also thank Melissa McClure and Manoj Puravankara for providing IRS spectra of objects in Ophiuchus and Chamaeleon, and Greg Schwarz for helping with the data formatting. This material is based upon work supported by the National Science Foundation under Grant No. AST-1455042. It is also funded by *Herschel* Grant No. JPL RSA 1500040. D.A.N. and M.H.D.vdW. acknowledge support from the CSA and NSERC. PACS has been developed by a consortium of institutes led by MPE (Germany) and including UVIE (Austria); KU Leuven, CSL, IMEC

(Belgium); CEA, LAM (France); MPIA (Germany); INAF-IFSI/OAA/OAP/OAT, LENS, SISSA (Italy); IAC (Spain). This development has been supported by the funding agencies BMVIT (Austria), ESA-PRODEX (Belgium), CEA/CNES (France), DLR (Germany), ASI/INAF (Italy), and CICYT/MCYT (Spain). SPIRE has been developed by a consortium of institutes led by Cardiff University (UK) and including Univ. Lethbridge (Canada); NAOC (China); CEA, LAM (France); IFSI, Univ. Padua (Italy); IAC (Spain); Stockholm Observatory (Sweden); Imperial College London, RAL, UCL-MSSL, UKATC, Univ. Sussex (UK); and Caltech, JPL, NHSC, Univ. Colorado (USA). This development has been supported by national funding agencies: CSA (Canada); NAOC (China); CEA, CNES, CNRS (France); ASI (Italy); MCINN (Spain); SNSB (Sweden); STFC, UKSA (UK); and NASA (USA). The CMC15 Data Access Service is the result of a collaboration agreement between the Centro de Astrobiología (CAB, INTA-CSIC) and the Real Instituto y Observatorio de la Armada en San Fernando (ROA). It has been developed in the framework of the Spanish Virtual Observatory project, supported by the Spanish MINECO through grant AYA 2011-14052 and the CoSADIE FP7 project (Call INFRA-2012-3.3 Research Infrastructures, project 312559). The system is maintained by the Data Archive Unit of the CAB (CSIC -INTA). Based on data from CMC15 Data Access Service at CAB (INTA-CSIC). Funding for SDSS-III has been provided by the Alfred P. Sloan Foundation, the Participating Institutions, the National Science Foundation, and the U.S. Department of Energy Office of Science. The SDSS-III web site is <http://www.sdss3.org/>. SDSS-III is managed by the Astrophysical Research Consortium for the Participating Institutions of the SDSS-III Collaboration including the University of Arizona, the Brazilian Participation Group, Brookhaven National Laboratory, Carnegie Mellon University, University of Florida, the French Participation Group, the German Participation Group, Harvard University, the Instituto de Astrofísica de Canarias, the Michigan State/Notre Dame/JINA Participation Group, Johns Hopkins University, Lawrence Berkeley National Laboratory, Max Planck Institute for Astrophysics, Max Planck Institute for Extraterrestrial Physics, New Mexico State University, New York University, Ohio State University, Pennsylvania State University, University of Portsmouth, Princeton University, the Spanish Participation Group, University of Tokyo, University of Utah, Vanderbilt University, University of Virginia, University of Washington, and Yale University.

*Software:* HIPE v14 ([Ott 2010](#)), emcee ([Foreman-Mackey et al. 2013](#)), Matplotlib ([Hunter 2007](#)), SciPy ([Jones et al. 2001](#)), Numpy ([van der Walt et al. 2011](#)), pandas ([Jones et al. 2001](#))

## REFERENCES

- Adachi, I., Hayashi, C., & Nakazawa, K. 1976, *Progress of Theoretical Physics*, 56, 1756
- Ahn, C. P., Alexandroff, R., Allende Prieto, C., et al. 2012, *ApJS*, 203, 21
- Alexander, R., Pascucci, I., Andrews, S., Armitage, P., & Cieza, L. 2014, *Protostars and Planets VI*, 475
- Allard, F., Homeier, D., & Freytag, B. 2012, *Royal Society of London Philosophical Transactions Series A*, 370, 2765
- ALMA Partnership, Brogan, C. L., Pérez, L. M., et al. 2015, *ApJL*, 808, L3
- Andre, P., & Montmerle, T. 1994, *ApJ*, 420, 837
- André, P., Men'shchikov, A., Bontemps, S., et al. 2010, *A&A*, 518, L102
- Andrews, S. M., Rosenfeld, K. A., Kraus, A. L., & Wilner, D. J. 2013, *ApJ*, 771, 129
- Andrews, S. M., & Williams, J. P. 2005, *ApJ*, 631, 1134
- . 2007, *ApJ*, 671, 1800
- Andrews, S. M., Wilner, D. J., Espaillat, C., et al. 2011, *ApJ*, 732, 42
- Andrews, S. M., Wilner, D. J., Hughes, A. M., Qi, C., & Dullemond, C. P. 2010, *ApJ*, 723, 1241
- Baraffe, I., Homeier, D., Allard, F., & Chabrier, G. 2015, *A&A*, 577, A42
- Beckwith, S. V. W., & Sargent, A. I. 1991, *ApJ*, 381, 250
- Beckwith, S. V. W., Sargent, A. I., Chini, R. S., & Guesten, R. 1990, *AJ*, 99, 924
- Belloche, A., Schuller, F., Parise, B., et al. 2011, *A&A*, 527, A145
- Birnstiel, T., Dullemond, C. P., & Brauer, F. 2010, *A&A*, 513, A79
- Brauer, F., Dullemond, C. P., Johansen, A., et al. 2007, *A&A*, 469, 1169
- Brown, J. M., Blake, G. A., Dullemond, C. P., et al. 2007, *ApJL*, 664, L107
- Bustamante, I., Merín, B., Ribas, Á., et al. 2015, *A&A*, 578, A23
- Calvet, N., D'Alessio, P., Hartmann, L., et al. 2002, *ApJ*, 568, 1008
- Calvet, N., Magris, G. C., Patino, A., & D'Alessio, P. 1992, *RMxAA*, 24, 27
- Chiang, E. I., & Goldreich, P. 1997, *ApJ*, 490, 368
- Cieza, L. A., Olofsson, J., Harvey, P. M., et al. 2013, *ApJ*, 762, 100
- D'Alessio, P., Calvet, N., & Hartmann, L. 2001, *ApJ*, 553, 321
- D'Alessio, P., Calvet, N., Hartmann, L., Franco-Hernández, R., & Servín, H. 2006, *ApJ*, 638, 314
- D'Alessio, P., Calvet, N., Hartmann, L., Lizano, S., & Cantó, J. 1999, *ApJ*, 527, 893
- D'Alessio, P., Cantó, J., Calvet, N., & Lizano, S. 1998, *ApJ*, 500, 411
- Davis, S. S. 2005, *ApJL*, 627, L153
- Dent, W. R. F., Thi, W. F., Kamp, I., et al. 2013, *PASP*, 125, 477
- Draine, B. T. 2006, *ApJ*, 636, 1114
- Dullemond, C. P., Dominik, C., & Natta, A. 2001, *ApJ*, 560, 957
- Dzib, S. A., Loinard, L., Mioduszewski, A. J., et al. 2013, *ApJ*, 775, 63
- Espaillat, C., Furlan, E., D'Alessio, P., et al. 2011, *ApJ*, 728, 49
- Espaillat, C., Muzerolle, J., Najita, J., et al. 2014, *Protostars and Planets VI*, 497
- Evans, II, N. J., Dunham, M. M., Jørgensen, J. K., et al. 2009, *ApJS*, 181, 321
- Foreman-Mackey, D., Hogg, D. W., Lang, D., & Goodman, J. 2013, *PASP*, 125, 306
- Forrest, W. J., Sargent, B., Furlan, E., et al. 2004, *ApJS*, 154, 443
- Fulton, T., Naylor, D. A., Polehampton, E. T., et al. 2016, *MNRAS*, 458, 1977
- Furlan, E., Calvet, N., D'Alessio, P., et al. 2005, *ApJL*, 628, L65
- Furlan, E., Hartmann, L., Calvet, N., et al. 2006, *ApJS*, 165, 568
- Furlan, E., Watson, D. M., McClure, M. K., et al. 2009, *ApJ*, 703, 1964
- Furlan, E., Luhman, K. L., Espaillat, C., et al. 2011, *The Astrophysical Journal Supplement Series*, 195, 3
- Goodman, J., & Weare, J. 2010, *Comm. App. Math. Comp. Sci.*, 5, 65
- Graciá-Carpio, J., Wetzstein, M., & Roussel, H. 2015, *ArXiv e-prints*, arXiv:1512.03252
- Guilloteau, S., Piétu, V., Chapillon, E., et al. 2016, *A&A*, 586, L1
- Haisch, Jr., K. E., Lada, E. A., & Lada, C. J. 2001, *ApJL*, 553, L153
- Henden, A. A., Templeton, M., Terrell, D., et al. 2016, *VizieR Online Data Catalog*, 2336
- Henning, T., Pfau, W., Zinnecker, H., & Prusti, T. 1993, *A&A*, 276, 129
- Herczeg, G. J., & Hillenbrand, L. A. 2015, *ApJ*, 808, 23
- Hernández, J., Calvet, N., Briceño, C., et al. 2007, *ApJ*, 671, 1784
- Hildebrand, R. H. 1983, *QJRAS*, 24, 267
- Houck, J. R., Roellig, T. L., van Cleve, J., et al. 2004, *ApJS*, 154, 18
- Howard, C. D., Sandell, G., Vacca, W. D., et al. 2013, *ApJ*, 776, 21
- Hunter, J. D. 2007, *Computing In Science & Engineering*, 9, 90
- Ireland, M. J., & Kraus, A. L. 2008, *ApJL*, 678, L59
- Ishihara, D., Onaka, T., Kataza, H., et al. 2010, *A&A*, 514, A1+
- Jones, E., Oliphant, T., Peterson, P., et al. 2001, *SciPy: Open source scientific tools for Python*, , [Online; accessed {today}]
- Kenyon, S. J., & Hartmann, L. 1987, *ApJ*, 323, 714
- Kessler-Silacci, J., Augereau, J.-C., Dullemond, C. P., et al. 2006, *ApJ*, 639, 275
- Lebouteiller, V., Barry, D. J., Goes, C., et al. 2015, *ApJS*, 218, 21
- Lebouteiller, V., Barry, D. J., Spoon, H. W. W., et al. 2011, *ApJS*, 196, 8
- Lommen, D., Wright, C. M., Maddison, S. T., et al. 2007, *A&A*, 462, 211
- Lommen, D. J. P., van Dishoeck, E. F., Wright, C. M., et al. 2010, *A&A*, 515, A77
- Luhman, K. L. 2007, *ApJS*, 173, 104
- Luhman, K. L., Allen, L. E., Allen, P. R., et al. 2008, *ApJ*, 675, 1375
- Manoj, P., Kim, K. H., Furlan, E., et al. 2011, *ApJS*, 193, 11
- Marchili, N., Hopwood, R., Fulton, T., et al. 2017, *MNRAS*, 464, 3331
- Mathews, G. S., Pinte, C., Duchêne, G., Williams, J. P., & Ménard, F. 2013, *A&A*, 558, A66
- Mathis, J. S. 1990, *ARA&A*, 28, 37
- Mathis, J. S., Rumpl, W., & Nordsieck, K. H. 1977, *ApJ*, 217, 425
- McClure, M. 2009, *ApJL*, 693, L81
- McClure, M. K., Furlan, E., Manoj, P., et al. 2010, *ApJS*, 188, 75
- Merín, B., Brown, J. M., Oliveira, I., et al. 2010, *ApJ*, 718, 1200
- Miyake, K., & Nakagawa, Y. 1993, *Icarus*, 106, 20
- Morales-Calderón, M., Stauffer, J. R., Hillenbrand, L. A., et al. 2011, *ApJ*, 733, 50
- Murakami, H., Baba, H., Barthel, P., et al. 2007, *PASJ*, 59, 369
- Muto, T., Grady, C. A., Hashimoto, J., et al. 2012, *ApJL*, 748, L22
- Muzerolle, J., Calvet, N., Hartmann, L., & D'Alessio, P. 2003, *ApJL*, 597, L149

- Natta, A., Testi, L., Calvet, N., et al. 2007, *Protostars and Planets V*, 767
- Natta, A., Testi, L., Neri, R., Shepherd, D. S., & Wilner, D. J. 2004, *A&A*, 416, 179
- Olofsson, J., Szűcs, L., Henning, T., et al. 2013, *A&A*, 560, A100
- Ortiz-León, G. N., Loinard, L., Kounkel, M. A., et al. 2017, *ApJ*, 834, 141
- Osorio, M., Macías, E., Anglada, G., et al. 2016, *ApJL*, 825, L10
- Ott, S. 2010, in *Astronomical Society of the Pacific Conference Series*, Vol. 434, *Astronomical Data Analysis Software and Systems XIX*, ed. Y. Mizumoto, K.-I. Morita, & M. Ohishi, 139
- Pascucci, I., Gorti, U., & Hollenbach, D. 2012, *ApJL*, 751, L42
- Pascucci, I., Testi, L., Herczeg, G. J., et al. 2016, *ApJ*, 831, 125
- Pearson, C., Lim, T., North, C., et al. 2014, *Experimental Astronomy*, 37, 175
- Pecaut, M. J., & Mamajek, E. E. 2013, *ApJS*, 208, 9
- Pecaut, M. J., Mamajek, E. E., & Bubar, E. J. 2012, *ApJ*, 746, 154
- Piétu, V., Guilloteau, S., Di Folco, E., Dutrey, A., & Boehler, Y. 2014, *A&A*, 564, A95
- Pilbratt, G. L., Riedinger, J. R., Passvogel, T., et al. 2010, *A&A*, 518, L1
- Pinilla, P., Birnstiel, T., Ricci, L., et al. 2012, *A&A*, 538, A114
- Preibisch, T., Brown, A. G. A., Bridges, T., Guenther, E., & Zinnecker, H. 2002, *AJ*, 124, 404
- Rebollido, I., Merín, B., Ribas, Á., et al. 2015, *A&A*, 581, A30
- Ribas, Á., Bouy, H., & Merín, B. 2015, *A&A*, 576, A52
- Ribas, Á., Merín, B., Bouy, H., et al. 2013, *A&A*, 552, A115
- Ricci, L., Testi, L., Natta, A., & Brooks, K. J. 2010a, *A&A*, 521, A66
- Ricci, L., Testi, L., Natta, A., et al. 2010b, *A&A*, 512, A15
- . 2014, *ApJ*, 791, 20
- Riviere-Marichalar, P., Merín, B., Kamp, I., Eiroa, C., & Montesinos, B. 2016, *A&A*, 594, A59
- Rodmann, J., Henning, T., Chandler, C. J., Mundy, L. G., & Wilner, D. J. 2006, *A&A*, 446, 211
- Siess, L., Dufour, E., & Forestini, M. 2000, *A&A*, 358, 593
- Skrutskie, M. F., Cutri, R. M., Stiening, R., et al. 2006, *The Astronomical Journal*, 131, 1163
- Spezzi, L., Cox, N. L. J., Prusti, T., et al. 2013, *A&A*, 555, A71
- Strom, K. M., Strom, S. E., Edwards, S., Cabrit, S., & Skrutskie, M. F. 1989, *AJ*, 97, 1451
- Takeuchi, T., & Lin, D. N. C. 2002, *ApJ*, 581, 1344
- . 2005, *ApJ*, 623, 482
- Testi, L., Natta, A., Scholz, A., et al. 2016, *A&A*, 593, A111
- Testi, L., Birnstiel, T., Ricci, L., et al. 2014, *Protostars and Planets VI*, 339
- Torres, R. M., Loinard, L., Mioduszewski, A. J., & Rodríguez, L. F. 2007, *ApJ*, 671, 1813
- Ubach, C., Maddison, S. T., Wright, C. M., et al. 2012, *MNRAS*, 425, 3137
- Valtchanov, I., Hopwood, R., Polehampton, E., et al. 2014, *Experimental Astronomy*, 37, 207
- van der Marel, N., van Dishoeck, E. F., Bruderer, S., et al. 2013, *Science*, 340, 1199
- van der Plas, G., Wright, C. M., Ménard, F., et al. 2017, *A&A*, 597, A32
- van der Walt, S., Colbert, S. C., & Varoquaux, G. 2011, *Computing in Science Engineering*, 13, 22
- Walsh, C., Juhász, A., Meeus, G., et al. 2016, *ApJ*, 831, 200
- Weidenschilling, S. J. 1977, *Ap&SS*, 51, 153
- Whittet, D. C. B., Prusti, T., Franco, G. A. P., et al. 1997, *A&A*, 327, 1194
- Wilking, B. A., Gagné, M., & Allen, L. E. 2008, *Star Formation in the  $\rho$  Ophiuchi Molecular Cloud*, ed. B. Reipurth, 351
- Winston, E., Cox, N. L. J., Prusti, T., et al. 2012, *A&A*, 545, A145
- Wright, E. L., Eisenhardt, P. R. M., Mainzer, A. K., et al. 2010, *The Astronomical Journal*, 140, 1868
- Zhu, Z., Nelson, R. P., Hartmann, L., Espaillat, C., & Calvet, N. 2011, *ApJ*, 729, 47

## APPENDIX

## A. HERSCHEL OBSERVATIONS USED IN THIS STUDY

**Table A1.** Summary of *Herschel* OBSIDs of Large Maps

OBSID pair	Wavelengths ( $\mu\text{m}$ )	Central Coordinates	
		(hh:mm:ss)	(dd:mm:ss)
Taurus			
1342202088, 1342202089	PACS: 70, 160	04 03 59	+26 17 52
	SPIRE: 250, 350, 500	04 04 44	+26 20 01
1342190617, 1342190618	PACS: 70, 160	04 13 07	+25 01 43
	SPIRE: 250, 350, 500	04 12 20	+25 00 05
1342202254, 1342202090*	PACS: 70, 160	04 15 05	+28 27 06
	SPIRE: 250, 350, 500	04 15 51	+28 28 24
1342216549, 1342216550	PACS: 100, 160	04 16 29	+28 22 56
1342204860, 1342204861	PACS: 70, 160	04 20 38	+25 13 03
	SPIRE: 250, 350, 500	04 21 23	+25 14 33
1342227304, 1342227305	PACS: 100, 160	04 21 21	+25 14 14
1342202254, 1342190616*	PACS: 70, 160	04 25 40	+27 13 29
	SPIRE: 250, 350, 500	04 24 54	+27 11 58
1342202250, 1342202251	PACS: 70, 160	04 28 45	+18 31 00
	SPIRE: 250, 350, 500	04 29 29	+18 33 11
1342190654, 1342190655	PACS: 70, 160	04 32 01	+24 26 31
	SPIRE: 250, 350, 500	04 31 15	+24 25 05
1342228005, 1342228006	PACS: 100, 160	04 31 16	+24 25 06
1342239280, 1342239281	PACS: 70, 160	04 34 22	+25 13 23
	SPIRE: 250, 350, 500	04 33 38	+25 12 29
1342190652, 1342190653	PACS: 70, 160	04 35 49	+23 01 41
	SPIRE: 250, 350, 500	04 35 00	+23 00 04
1342202252, 1342202253	PACS: 70, 160	04 36 49	+26 00 28
	SPIRE: 250, 350, 500	04 37 30	+26 01 15
1342228174, 1342228175	PACS: 100, 160	04 38 25	+25 50 14
1342204843, 1342204844	PACS: 70, 160	04 52 35	+30 45 29
	SPIRE: 250, 350, 500	04 53 26	+30 46 25
1342204841, 1342204842	PACS: 70, 160	05 01 00	+25 53 28
	SPIRE: 250, 350, 500	05 01 46	+25 54 56
Ophiuchus			
1342205093, 1342205094	PACS: 70, 160	16 27 28	-24 12 03
	SPIRE: 250, 350, 500	16 26 45	-24 11 15
1342227148, 1342227149	PACS: 100, 160	16 26 23	-24 12 09
1342238816, 1342238817	PACS: 70, 160	16 27 06	-24 28 42
Chamaeleon			
1342213178, 1342213179	PACS: 70, 160	10 58 56	-77 10 45
	SPIRE: 250, 350, 500	11 01 03	-77 18 50
1342224782, 1342224783	PACS: 100, 160	11 07 48	-77 25 01

\*: obsids 1342202254 (scan), 1342202090 (cross scan 1), 1342190616 (cross scan 2) covered a similar region, but were processed separately as two sub-maps due to processing limitations, each of them being one scan + cross scan combination.



**Table A2.** Additional *Herschel* Observations of Sources Outside Large Maps

Object	OBSIDs	Wavelengths	Object Coordinates	
		( $\mu\text{m}$ )	(hh:mm:ss)	(dd:mm:ss)
2MASS J04390525+2337450	1342243086, 1342243087	70, 160	04 39 05	+23 37 45
2MASS J04393364+2359212	1342243438, 1342243439	70, 160	04 39 34	+23 59 21
2MASS J04400067+2358211	1342243436, 1342243437	70, 160	04 40 01	+23 58 21
CoKu Tau/4	1342193136	70, 160*	04 41 17	+28 40 00
	1342217520, 1342217521	100, 160*		
CX Tau	1342216545, 1342216546	70, 160	04 14 48	+26 48 11
	1342216547, 1342216548	100, 160		
DQ Tau	1342217462, 1342217463	70, 160	04 46 53	+17 00 00
	1342217464, 1342217465	100, 160		
DS Tau	1342193135	70, 160	04 47 49	+29 25 11
	1342217518, 1342217519	100, 160		
FP Tau	1342216545, 1342216546	70, 160	04 14 47	+26 46 26
	1342216547, 1342216548	100, 160		
Haro 6-37	1342193141	70, 160	04 46 59	+17 02 38
	1342217466, 1342217467	100, 160		
LkCa 15	1342217470, 1342217471	70, 160	04 39 18	+22 21 04
	1342217472, 1342217473	100, 160		
RW Aur	1342193130	70, 160	05 07 50	+30 24 05
	1342217508, 1342217509	100, 160		

\*: 160  $\mu\text{m}$  flux measurements were discarded in the case of CoKu/Tau 4 due to extended emission.

NOTE—For single observations, only one OBSID is listed.

**Table A3.** SPIRE FTS spectra Used (after Quality Check)

Name	OBSIDs
16156-2358AB	1342242600
16201-2410	1342262850
AA Tau	1342265818
CI Tau	1342265815
CR Cha	1342257313
CS Cha	1342257315
CU Cha	1342224750
CW Tau	1342249051
DG Tau	1342265852
DL Tau	1342265849
DOAR25	1342262851
DQ Tau	1342228736
DR Tau	1342243598
GG Tau	1342265813
GM Aur	1342228740
Haro 6-37	1342228737

Table A3 continued

Table A3 (*continued*)

Name	OBSIDs
IRAS 04385+2550	1342243595
IRS48	1342262840
LkCa 15	1342265848
ROX-44	1342262828
RW Aur	1342243599
SR21AB	1342262844
SU Aur	1342228741
SZ Cha	1342257314
T33A	1342224749
T42	1342248248
T56	1342248247
UX Tau A+C	1342249050
UY Aur	1342228742
UZ Tau A	1342265857
V892 Tau	1342265825
WSB60	1342262834
WW Cha	1342257327
ZZ Tau IRS	1342265850

**Table A4.** SPIRE FTS Spectra (Non-detections and Those Discarded after Quality Check).

Name	OBSIDs
BP Tau	1342250506
CIDA 9	1342227782
CY Tau	1342250504
DD Tau	1342250505
DE Tau	1342250507
DH Tau	1342265854
DK Tau	1342265856
DM Tau	1342265814
DN Tau	1342265817
DO Tau	1342265859
FN Tau	1342250503
FQ Tau	1342239355
FS Tau	1342250502
FT Tau	1342265823
FV Tau	1342265851
FX Tau	1342265822

*Table A4 continued*

Table A4 (*continued*)

Name	OBSIDs
GH Tau	1342250496
GI Tau	1342250498
GK Tau	1342265819
GO Tau	1342243597
Haro 6-13	1342265820
GY314	1342262838
HK Tau	1342265821
HP Tau	1342227449
IRAS 04154+2823	1342265826
IRAS 04216+2603	1342250501
IRAS 04260+2642	1342265853
IP Tau	1342265824
IQ Tau	1342265855
MHO 3	1342249052
V710 Tau	1342250495
V807 Tau	1342250497
V836 Tau	1342227783
16193-2314	1342251283
DOAR16AB	1342262825
16225-2607	1342262853
DOAR21	1342262849
DOAR24	1342262848
GSS39	1342262846
DOAR28	1342262824
IRS49	1342262839
GY314	1342262838
16289-2457	1342262833
ROX-43A1	1342262829
SX Cha	1342251309
TW Cha	1342248245
CT Cha	1342231974
ISO 52	1342257316
T21	1342257318
CHXR 20	1342231082
UY Cha	1342257319
UZ Cha	1342257332
CHXR 22E	1342251310
T25	1342231973
CHXR 30B	1342257320
VW Cha	1342224752
T35	1342257321
VZ Cha	1342257331
C7-1	1342231081

*Table A4 continued*

Table A4 (*continued*)

---

---

Name	OBSIDs
B43	1342231080
T43	1342257330
WX Cha	1342257317
WY Cha	1342257329
Hn 11	1342257328
T47	1342257322
WZ Cha	1342257326
XX Cha	1342251291
T51	1342257325
CV Cha	1342257324
T54	1342257323
2M J11241186-7630425	1342243638

---

## B. HERSCHEL PHOTOMETRY

**Table B5.** *Herschel* Photometry Obtained in this Study

Name	R.A. (hh:mm:ss)	Decl. (dd:mm:s)	$F_{70\mu\text{m}}$ (mJy)	$F_{100\mu\text{m}}$ (mJy)	$F_{160\mu\text{m}}$ (mJy)	$F_{250\mu\text{m}}$ (mJy)	$F_{350\mu\text{m}}$ (mJy)	$F_{500\mu\text{m}}$ (mJy)
IRAS 04108+2910	04:13:57.38	+29:18:19.3	500±100	...	290±60	170±30	110±20	70±10
V773 Tau	04:14:12.92	+28:12:12.4	800±200	500±100	310±60	...	...	...
FM Tau	04:14:13.58	+28:12:49.2	500±100	330±70	280±60	130±30	...	...
FN Tau	04:14:14.59	+28:27:58.1	1500±300	1100±200	700±100	390±80	200±40	110±20
CW Tau	04:14:17.00	+28:10:57.8	1900±400	2000±400	1800±400	1300±300	800±200	...
CIDA 1	04:14:17.61	+28:06:09.7	300±60	410±80	250±50	...	...	...
MHO 3	04:14:30.55	+28:05:14.7	3700±700	3100±600	3500±700	...	...	...
FP Tau	04:14:47.31	+26:46:26.4	330±70	380±80	420±80	...	...	...
CX Tau	04:14:47.86	+26:48:11.0	310±60	260±50	240±50	...	...	...
FO Tau	04:14:49.29	+28:12:30.6	500±100	470±90	120±20	...	...	...
2MASS J04153916+2818586	04:15:39.16	+28:18:58.6	500±100	450±90	500±100	280±60	210±40	180±40
IRAS 04125+2902	04:15:42.78	+29:09:59.7	1300±300	1300±300	1000±200	700±100	380±80	200±40
CY Tau	04:17:33.73	+28:20:46.9	260±50	210±40	280±60	400±80	340±70	250±50
KPNO 10	04:17:49.55	+28:13:31.9	120±20	150±30	...	...	...	...
DD Tau	04:18:31.13	+28:16:29.0	1200±200	1100±200	700±100	370±70	230±50	130±30
CZ Tau	04:18:31.59	+28:16:58.5	380±80	100±20	...	...	...	...
IRAS 04154+2823	04:18:32.03	+28:31:15.4	1400±300	1600±300	1200±200	800±200	600±100	...
V410 X-ray 2	04:18:34.44	+28:30:30.2	800±200	600±100	470±90	370±70	...	...
V892 Tau	04:18:40.62	+28:19:15.5	50000±10000	40000±8000	23000±5000	9000±2000	5000±1000	2100±400
LR 1	04:18:41.33	+28:27:25.0	800±200	1000±200	1200±200	900±200	600±100	500±100
V410 X-ray 6	04:19:01.11	+28:19:42.0	500±100	430±90	500±100	...	...	...
FQ Tau	04:19:12.81	+28:29:33.1	...	190±40	150±30	...	...	...
BP Tau	04:19:15.84	+29:06:26.9	600±100	...	500±100	500±100	400±80	300±60
IRAS 04173+2812	04:20:25.84	+28:19:23.6	250±50	90±20	...	...	...	...
2MASS J04202606+2804089	04:20:26.07	+28:04:09.0	320±60	...	190±40	47±9	...	...
2MASS J04210795+2702204	04:21:07.95	+27:02:20.4	3200±600	...	3700±700	1600±300	1500±300	1500±300
DE Tau	04:21:55.64	+27:55:06.1	1300±300	...	800±200	400±80	270±50	140±30
RY Tau	04:21:57.40	+28:26:35.5	14000±3000	...	9000±2000	5000±1000	3200±600	1800±400
IRAS F04192+2647	04:22:16.76	+26:54:57.1	350±70	...	...	...	...	...
IRAS 04196+2638	04:22:47.87	+26:45:53.0	500±100	...	430±90	340±70	300±60	220±40
IRAS 04200+2759	04:23:07.77	+28:05:57.3	500±100	...	270±50	230±50	220±40	160±30
FT Tau	04:23:39.19	+24:56:14.1	800±200	1000±200	1200±200	1000±200	800±200	600±100
IRAS 04216+2603	04:24:44.58	+26:10:14.1	800±200	...	1000±200	700±100	470±90	310±60
IP Tau	04:24:57.08	+27:11:56.5	500±100	...	160±30	200±40	130±30	110±20
FV Tau	04:26:53.53	+26:06:54.4	1700±300	...	1000±200	...	...	...
DF Tau	04:27:02.80	+25:42:22.3	700±100	...	120±20	70±10	...	...
DG Tau	04:27:04.70	+26:06:16.3	21000±4000	...	16000±3000	8000±2000	5000±1000	2900±600
IRAS 04260+2642	04:29:04.98	+26:49:07.3	1100±200	...	1500±300	1000±200	800±200	470±90
IRAS 04263+2654	04:29:21.65	+27:01:25.9	350±70	...	...	...	...	...
XEST 13-010	04:29:36.07	+24:35:55.7	250±50	200±40	260±50	...	...	...
DH Tau	04:29:41.56	+26:32:58.3	500±100	...	500±100	330±70	240±50	140±30
IQ Tau	04:29:51.56	+26:06:44.9	800±200	...	900±200	800±200	700±100	500±100
2MASS J04295950+2433078	04:29:59.51	+24:33:07.8	...	47±9	13±3	...	...	...
UX Tau A+C	04:30:04.00	+18:13:49.4	3300±700	...	2600±500	1700±300	1000±200	500±100
FX Tau	04:30:29.61	+24:26:45.0	350±70	240±50	170±30	100±20	...	...
DK Tau	04:30:44.25	+26:01:24.5	1200±200	...	900±200	600±100	360±70	240±50
IRAS 04278+2253	04:30:50.28	+23:00:08.8	...	...	...	1100±200	600±100	470±90
ZZ Tau IRS	04:30:51.71	+24:41:47.5	3800±800	3100±600	3300±700	2600±500	2100±400	1500±300

*Table B5 continued*

Table B5 (*continued*)

Name	R.A. (hh:mm:ss)	Decl. (dd:mm:s)	$F_{70\ \mu\text{m}}$ (mJy)	$F_{100\ \mu\text{m}}$ (mJy)	$F_{160\ \mu\text{m}}$ (mJy)	$F_{250\ \mu\text{m}}$ (mJy)	$F_{350\ \mu\text{m}}$ (mJy)	$F_{500\ \mu\text{m}}$ (mJy)
XZ Tau	04:31:40.07	+18:13:57.2	8000±2000	...	...	...	...	...
HK Tau	04:31:50.57	+24:24:18.1	2600±500	2600±500	2100±400	1400±300	900±200	500±100
V710 Tau	04:31:57.80	+18:21:35.1	290±60	...	700±100	700±100	500±100	370±70
Haro 6-13	04:32:15.41	+24:28:59.7	8000±2000	8000±2000	7000±1000	4100±800	2700±500	2100±400
MHO 6	04:32:22.11	+18:27:42.6	...	...	180±40	190±40	170±30	110±20
UZ Tau A	04:32:43.04	+25:52:31.1	2200±400	...	2100±400	1600±300	1300±300	900±200
JH 112 A	04:32:49.11	+22:53:02.8	600±100	...	440±90	...	...	...
V807 Tau	04:33:06.64	+24:09:55.0	700±100	700±100	600±100	190±40	150±30	100±20
IRAS 04303+2240	04:33:19.07	+22:46:34.2	1600±300	...	700±100	320±60	...	...
2MASS J04333905+2227207	04:33:39.05	+22:27:20.7	320±60	...	500±100	430±90	350±70	260±50
DL Tau	04:33:39.06	+25:20:38.2	1300±300	...	1900±400	2000±400	1800±400	...
HN Tau	04:33:39.35	+17:51:52.4	...	...	...	280±60	190±40	100±20
2MASS J04334465+2615005	04:33:44.65	+26:15:00.5	...	170±30	280±60	230±50	...	...
DM Tau	04:33:48.72	+18:10:10.0	...	...	...	800±200	700±100	600±100
CI Tau	04:33:52.00	+22:50:30.2	1900±400	...	2000±400	2000±400	1800±400	1300±300
IT Tau	04:33:54.70	+26:13:27.5	300±60	350±70	430±90	180±40	110±20	...
AA Tau	04:34:55.42	+24:28:53.2	1300±300	1000±200	1200±200	1100±200	900±200	600±100
HO Tau	04:35:20.20	+22:32:14.6	...	...	...	140±30	120±20	90±20
DN Tau	04:35:27.37	+24:14:58.9	700±100	800±200	800±200	600±100	500±100	400±80
HQ Tau	04:35:47.34	+22:50:21.7	1400±300	...	600±100	200±40	70±10	...
2MASS J04381486+2611399	04:38:14.87	+26:11:39.7	...	50±10	...	...	...	...
DO Tau	04:38:28.58	+26:10:49.4	6000±1000	6000±1000	5000±1000	2500±500	1800±400	1300±300
2MASS J04390525+2337450	04:39:05.25	+23:37:45.0	420±80	...	340±70	...	...	...
VY Tau	04:39:17.41	+22:47:53.4	240±50	...	220±40	...	...	...
LkCa 15	04:39:17.80	+22:21:03.5	1200±200	1500±300	1800±400	...	...	...
GN Tau	04:39:20.91	+25:45:02.1	100±20	170±30	...	...	...	...
2MASS J04393364+2359212	04:39:33.64	+23:59:21.2	80±20	...	60±10	...	...	...
ITG 15	04:39:44.88	+26:01:52.8	350±70	240±50	...	...	...	...
2MASS J04400067+2358211	04:40:00.68	+23:58:21.2	70±10	...	60±10	...	...	...
IRAS 04370+2559	04:40:08.00	+26:05:25.4	600±100	420±80	410±80	...	...	...
JH 223	04:40:49.51	+25:51:19.2	120±20	80±20	...	...	...	...
ITG 33A	04:41:08.26	+25:56:07.5	...	140±30	...	...	...	...
CoKu Tau/4	04:41:16.81	+28:40:00.1	1000±200	1100±200	...	...	...	...
IRAS 04385+2550	04:41:38.82	+25:56:26.8	2900±600	3000±600	2600±500	1300±300	700±100	...
CIDA 7	04:42:21.02	+25:20:34.4	310±60	400±80	410±80	230±50	130±30	90±20
DP Tau	04:42:37.70	+25:15:37.5	600±100	340±70	150±30	...	...	...
GO Tau	04:43:03.09	+25:20:18.8	370±70	380±80	600±100	600±100	600±100	500±100
DQ Tau	04:46:53.05	+17:00:00.2	1400±300	1500±300	900±200	...	...	...
Haro 6-37	04:46:58.98	+17:02:38.2	1100±200	1100±200	1300±300	...	...	...
DS Tau	04:47:48.59	+29:25:11.2	200±40	280±60	240±50	...	...	...
UY Aur	04:51:47.38	+30:47:13.5	6000±1000	...	3600±700	1500±300	700±100	370±70
GM Aur	04:55:10.98	+30:21:59.5	3100±600	...	4300±900	4300±900	3300±700	2000±400
AB Aur	04:55:45.83	+30:33:04.4	140000±30000	...	70000±10000	22000±4000	8000±2000	2500±500
V836 Tau	05:03:06.60	+25:23:19.7	340±70	...	430±90	320±60	240±50	140±30
CIDA 9	05:05:22.86	+25:31:31.2	450±90	...	600±100	450±90	330±70	210±40
RW Aur	05:07:49.54	+30:24:05.1	2500±500	2900±600	1500±300	...	...	...
16156-2358AB	16:18:37.25	-24:05:18.19	...	...	...	2500±500	1200±200	500±100
16193-2314	16:22:18.55	-23:21:45.36	1400±300	...	1400±300	700±100	450±90	250±50
16201-2410	16:23:09.23	-24:17:04.69	2400±500	2600±500	2100±400	1000±200	600±100	410±80
16220-2452AB	16:25:02.13	-24:59:31.85	900±200	500±100	440±90	290±60	160±30	100±20



Table B5 (*continued*)

Name	R.A. (hh:mm:ss)	Decl. (dd:mm:s)	$F_{70\ \mu\text{m}}$ (mJy)	$F_{100\ \mu\text{m}}$ (mJy)	$F_{160\ \mu\text{m}}$ (mJy)	$F_{250\ \mu\text{m}}$ (mJy)	$F_{350\ \mu\text{m}}$ (mJy)	$F_{500\ \mu\text{m}}$ (mJy)
DOAR16AB	16:25:10.45	-23:19:11.96	1300±300	1000±200	900±200	420±80	280±60	170±30
IRS2AB	16:25:36.75	-24:15:42.12	2100±400	...	...	...	...	...
16225-2607	16:25:38.48	-26:13:53.99	...	...	...	90±20	60±10	...
SR4	16:25:56.18	-24:20:48.22	8000±2000	10000±2000	8000±2000	...	...	...
DOAR24	16:26:17.09	-24:20:21.41	1200±200	...	...	...	...	...
GSS31AB	16:26:23.38	-24:20:59.69	5000±1000	7000±1000	...	...	...	...
DOAR25	16:26:23.678	-24:43:13.86	1800±400	3200±600	5000±1000	2800±600	2300±500	1500±300
GSS39	16:26:45.05	-24:23:07.72	...	...	1900±400	3400±700	2600±500	...
VSS27AB	16:26:46.44	-24:11:59.99	700±100	1300±300	...	...	...	...
DOAR28	16:26:47.49	-23:14:54.79	1000±200	1000±200	1000±200	800±200	600±100	400±80
16237-2349	16:26:48.66	-23:56:33.98	360±70	380±80	...	...	...	...
WL18AB	16:26:48.99	-24:38:25.1	600±100	1400±300	...	...	...	...
VSSG5AB	16:26:54.45	-24:26:20.56	70±10	...	...	...	...	...
GY204	16:27:06.61	-24:41:48.8	110±20	...	...	...	...	...
WL10	16:27:09.12	-24:34:08.29	900±200	600±100	340±70	...	...	...
SR21AB	16:27:10.28	-24:19:12.61	31000±6000	26000±5000	16000±3000	8000±2000	3900±800	1500±300
IRS36	16:27:15.9	-24:25:14.03	200±40	500±100	...	...	...	...
VSSG25AB	16:27:27.4	-24:31:16.57	600±100	700±100	...	...	...	...
GY289	16:27:32.67	-24:33:24.15	70±10	...	...	...	...	...
GY292	16:27:33.11	-24:41:15.14	2400±500	...	...	...	...	...
IRS48	16:27:37.18	-24:30:35.2	42000±8000	31000±6000	19000±4000	3700±700	1400±300	...
IRS49	16:27:38.31	-24:36:58.73	1400±300	1600±300	900±200	500±100	...	...
GY314	16:27:39.43	-24:39:15.51	2300±500	2700±500	3300±700	1100±200	500±100	...
SR9AB	16:27:40.28	-24:22:04.31	900±200	600±100	...	...	...	...
GY352	16:27:47.08	-24:45:34.79	60±10	...	...	...	...	...
GY397	16:27:55.24	-24:28:39.72	150±30	...	...	...	...	...
GY463	16:28:04.65	-24:34:56.15	39±8	...	...	...	...	...
WSB60	16:28:16.51	-24:36:57.95	900±200	1200±200	1000±200	1300±300	1000±200	...
ROX-42Cab	16:31:15.75	-24:34:02.21	220±40	320±60	...	...	...	...
ROX-43A1	16:31:20.12	-24:30:05.03	1100±200	900±200	280±60	180±40	...	...
IRS-60	16:31:30.88	-24:24:39.88	1200±200	...	800±200	390±80	230±50	70±10
ROX-44	16:31:33.45	-24:27:37.11	4300±900	...	2600±500	1500±300	900±200	500±100
16289-2457	16:31:54.74	-25:03:23.82	2000±400	...	...	...	...	...
SX Cha	10:55:59.73	-77:24:39.9	800±200	600±100	420±80	280±60	190±40	130±30
T5	10:57:42.20	-76:59:35.7	220±40	210±40	200±40	...	...	...
SZ Cha	10:58:16.77	-77:17:17.1	4000±800	3800±800	3600±700	2800±600	1900±400	1100±200
TW Cha	10:59:01.09	-77:22:40.7	420±80	340±70	400±80	310±60	210±40	110±20
CR Cha	10:59:06.99	-77:01:40.4	1600±300	2300±500	2700±500	2400±500	1800±400	1200±200
CS Cha	11:02:24.91	-77:33:35.7	3200±600	2900±600	2200±400	1400±300	900±200	500±100
CT Cha	11:04:09.09	-76:27:19.4	700±100	700±100	800±200	500±100	380±80	270±50
ISO 52	11:04:42.58	-77:41:57.1	...	200±40	...	...	...	...
UY Cha	11:06:59.07	-77:18:53.6	...	170±30	...	...	...	...
UZ Cha	11:07:12.07	-76:32:23.2	270±50	340±70	260±50	...	...	...
T25	11:07:19.15	-76:03:04.8	500±100	...	390±80	300±60	180±40	70±10
T28	11:07:43.66	-77:39:41.1	460±90	600±100	470±90	...	...	...
T29	11:07:57.93	-77:38:44.9	13000±3000	14000±3000	...	...	...	...
VW Cha	11:08:01.49	-77:42:28.8	1400±300	900±200	600±100	220±40	...	...
CU Cha	11:08:03.30	-77:39:17.4	120000±20000	70000±10000	60000±10000	39000±8000	24000±5000	12000±2000
T33A	11:08:15.10	-77:33:53.2	7000±1000	5000±1000	3900±800	2200±400	1300±300	600±100
T35	11:08:39.05	-77:16:04.2	400±80	320±60	160±30	120±20	...	...

*Table B5 continued*

Table B5 (*continued*)

Name	R.A. (hh:mm:ss)	Decl. (dd:mm:s)	$F70\ \mu\text{m}$ (mJy)	$F100\ \mu\text{m}$ (mJy)	$F160\ \mu\text{m}$ (mJy)	$F250\ \mu\text{m}$ (mJy)	$F350\ \mu\text{m}$ (mJy)	$F500\ \mu\text{m}$ (mJy)
VY Cha	11:08:54.64	-77:02:13.0	340±70	150±30	...	...	...	...
C1-6	11:09:22.67	-76:34:32.0	1500±300	1600±300	1600±300	...	...	...
VZ Cha	11:09:23.79	-76:23:20.8	410±80	350±70	370±70	430±90	360±70	270±50
B43	11:09:47.42	-77:26:29.1	200±40	160±30	340±70	360±70	350±70	250±50
T42	11:09:53.41	-76:34:25.5	15000±3000	19000±4000	17000±3000	...	...	...
T43	11:09:54.08	-76:29:25.3	400±80	500±100	...	...	...	...
WX Cha	11:09:58.74	-77:37:08.9	330±70	220±40	120±20	100±20	...	...
WW Cha	11:10:00.11	-76:34:57.9	27000±5000	37000±7000	30000±6000	15000±3000	9000±2000	5000±1000
T45a	11:10:07.04	-76:29:37.7	260±50	300±60	...	...	...	...
ISO 237	11:10:11.42	-76:35:29.3	2900±600	6000±1000	...	...	...	...
CHXR 47	11:10:38.02	-77:32:39.9	220±40	120±20	...	...	...	...
T47	11:10:49.60	-77:17:51.7	700±100	500±100	430±90	320±60	190±40	120±20
WZ Cha	11:10:53.34	-76:34:32.0	...	160±30	...	...	...	...
ISO 256	11:10:53.59	-77:25:00.5	...	40±8	...	...	...	...
XX Cha	11:11:39.66	-76:20:15.2	190±40	180±40	...	100±20	90±20	100±20
T50	11:12:09.85	-76:34:36.5	...	120±20	...	...	...	...
CV Cha	11:12:27.72	-76:44:22.3	2700±500	2200±400	1300±300	600±100	340±70	150±30
T56	11:17:37.01	-77:04:38.1	700±100	600±100	450±90	290±60	180±40	100±20

NOTE—The complete version of Tables 3, 5, 6, and B5 are merged together in the Zenodo repository, also available in machine readable format in the online journal.

**Table B6.** Objects with Nearby Sources/Extended Emission in *Herschel* Maps

Name	Notes
CoKu Tau/4	No flux estimate for $\lambda > 70 \mu\text{m}$ due to extended emission
FS Tau	Nearby source
FY Tau	Nearby source (FZ Tau)
FZ Tau	Nearby source (FY Tau)
GH Tau	Nearby source
GI Tau	Nearby source (GK Tau)
GK Tau	Nearby source (GI Tau)
Haro 6-5B	Nearby source
HP Tau	Extended emission/nearby source?
IC 2087 IR	Extended emission
ITG 40	Nearby source
JH 112 B	Emission attributed to the A component, based on SED
KPNO 10	No flux estimate for $\lambda > 100 \mu\text{m}$ , due to extended emission
LkHa 358	Nearby source
SU Aur	Extended emission / Nearby source?
V807 Tau	Nearby source, blended longward to $250 \mu\text{m}$
V955 Tau	Extended emission
IRS2AB	No flux estimate for $\lambda > 70 \mu\text{m}$ , due to extended emission
SR4	Background emission
DOAR21	Extended emission
VSSG1	Background emission
GY12	Extended emission
VSSG27AB	Background emission (no detection)
GSS37AB	Background emission
CRBR51	Background emission (no detection)
GY262	Nearby source
GY292	Extended emission
SR9AB	No flux estimate for $\lambda > 100 \mu\text{m}$ , due to extended emission
ROX-43A2	ROX-43 system unresolved in <i>Herschel</i> maps. <i>Herschel</i> fluxes assigned to A, based on its SED
T21	Extended emission
DI Cha	Extended emission
CHXR 30B	Nearby source (CHXR 30A)
T29	Nearby sources (measurements only at $70$ and $100 \mu\text{m}$ )
CHXR 30A	Nearby source (CHXR 30B)
C1-6	No flux estimate for $\lambda > 100 \mu\text{m}$ , due to extended emission
Hn 10E	Background emission (no detection)
HD 97300	Extended emission
XX Cha	No flux estimate for $\lambda > 100 \mu\text{m}$ due, to nearby source
T54	Extended emission

### C. SILICATE FEATURE CHARACTERIZATION

As mentioned in Sec. 3.4, the compiled IRS spectra were used to characterize the 10  $\mu\text{m}$  silicate feature of these disks when possible. Here, we describe the procedure in more detail.

We adopted the feature strength and shape definitions in [Furlan et al. \(2006\)](#) and [Kessler-Silacci et al. \(2006\)](#), respectively. The strength is defined as:

$$\text{Sil}_{\text{strength}} = \frac{\int (F_{\text{obs}} - F_{\text{cont}})d\lambda}{\int F_{\text{cont}}d\lambda} \quad (\text{C1})$$

where  $F_{\text{obs}}$  and  $F_{\text{cont}}$  are the observed and continuum fluxes, and the integral goes from 8 to 12.4  $\mu\text{m}$ , covering the extent of the 10  $\mu\text{m}$  feature. In the case of the silicate shape, a normalized spectrum ( $S_{\text{norm}}$ ) is first estimated:

$$S_{\text{norm}} = 1 + \frac{F_{\text{obs}} - F_{\text{cont}}}{\langle F_{\text{cont}} \rangle} \quad (\text{C2})$$

where  $\langle F_{\text{cont}} \rangle$  is the frequency-averaged continuum estimated from 5 to 16  $\mu\text{m}$  ([Kessler-Silacci et al. 2006](#)). The shape ( $\text{Sil}_{\text{shape}}$ ) is then the ratio of fluxes around 9.8 and 11.3 and 9.8  $\mu\text{m}$  ( $S_{11.3}/S_{9.8}$ ). The  $S_{11.3}$  and  $S_{9.8}$  fluxes were computed as the median flux for wavelengths  $\pm 0.2 \mu\text{m}$  around the central wavelengths, and only if at least three points were available to ensure a robust estimate. Following [Furlan et al. \(2011\)](#), this procedure was performed using the observed (i.e. not extinction-corrected) spectra. The value and uncertainties listed in Table 6 are the median, 16th and 84th percentiles of 1000 bootstrapping iterations, randomly changing flux values in the IRS spectra within their uncertainties. Given the uncertainty in estimating the continuum level (especially in the presence of strong silicate features), we followed a similar procedure as in [Furlan et al. \(2006, third-order polynomial fit\)](#) but allowed the polynomial degree to change from 3 to 5 during the bootstrapping, in order to account for this in the final uncertainty estimates.